Energy Advances

Accepted Manuscript

This article can be cited before page numbers have been issued, to do this please use: Y. Ranjith Kumar, K. Venkataramana and M. Vasundhara, *Energy Adv.*, 2026, DOI: 10.1039/D5YA00340G.

ROYAL SOCIETY OF CHEMISTRY

rsc.li/energy-advances

View Article Online
DOI: 10.1039/D5YA00340G

Natural Stabilizer-Assisted Sol-Gel Synthesis of Medium-Entropy Spinel Ferrite: Structural and Electrochemical Insights for Supercapacitor Applications

Y. Ranjith Kumar[a,b], Kasarapu Venkataramana[a], M. Vasundhara[a,b*]

[a]*Polymers and Functional Materials Department, CSIR-Indian Institute of Chemical Technology, Hyderabad-500007, India*
[b]*Academy of Scientific and Innovative Research (AcSIR), Ghaziabad-201002, India*

***Corresponding author email:** mvas@iict.res.in, **Contact No:** +91 9496445333

Abstract

Multi-cation spinel ferrites have gained significant interest due to their tuneable properties, enhanced stability, conductivity, and ion mobility, making them promising for supercapacitor applications. In the present study, (MnCoNiZn)Fe_2O_4 spinel ferrite was synthesized by sol-gel route using albumen (egg white) as natural stabilizer as well as chelating agent for the preparation of ferrite. The formation of single-phase cubic spinel structure with space group of *Fd-3m* has been established by XRD studies. The morphology analysis using FESEM and HRTEM revealed well-defined, uniformly distributed pyramidal-shaped particles, confirming the controlled growth achieved by the synthesis route. The optical band gap, determined from UV–Vis spectroscopy, is found to be 2.86 eV. The electrochemical evaluation was carried out in three electrode configuration using aqueous 2M KOH electrolytes. The prepared ferrite exhibited a specific capacitance as high as 408.18 F/g at a significantly high current density of 4 A/g in charge-discharging, highlighting its superior charge storage capacity. The coulombic efficiency has been found to be 91.6% upto 1500 continuous charge-discharge cycle which reveal excellent reversal behaviour. Additionally, a maximum energy density of 36.31 W h/kg is achieved at a power density of 1601.28 W/kg. Overall, this study establishes albumen-assisted sol-gel synthesis as a non-toxic stabilizer and effective strategy for producing medium-entropy spinel ferrites, emphasizing their potential as sustainable and high-performance electrode materials for superior performance supercapacitor applications.

Keywords: Medium-Entropy; Spinel Ferrite; Albumen; Sol-gel; Electrochemical; Supercapacitor;

View Article Online
DOI: 10.1039/D5YA00340G

1. Introduction

The rapidly advancing technologies of wearable electronics, electric transportation, and smart energy infrastructure have created demands for new sustainable, high efficiency energy storage systems that will accommodate the rising global demands for energy [1–4]. Among various energy storage technologies, supercapacitors (electrochemical capacitors) are perhaps the most important, filling the gap between traditional dielectric capacitors and rechargeable batteries [5–7]. The unique advantages of these devices, including ultrafast charge-discharge characteristics, superior power density, excellent rate performance, and outstanding cycling stability, make them indispensable for modern applications ranging from microelectronic sensors to hybrid electric vehicles [8–10]. However, despite of these advantages, the energy density of conventional supercapacitors is still low (less than 10 Wh/kg) and is thus a limiting factor in systems with high energy requirements. Accordingly, present work is directed toward new electrode materials which can be expected to impart high power and good energy density to the capacitive devices [11–13].

Transition metal oxides (TMOs) have emerged as promising pseudocapacitive materials due to their redox active sites, chemical versatility, and low cost [9,12,13]. Among them, ferrite-based oxides (MFe_2O_4) are particularly attractive owing to their structural stability, rich redox chemistry, and flexible spinel framework. The spinel structure, consisting of tetrahedral (A) and octahedral (B) sites, enables tunable cation distribution and multiple valence states, facilitating reversible Faradaic reactions and adjustable electronic properties [14–17]. All of these properties render ferrites very suitable for pseudocapacitor electrodes where rapid and reversible Faradaic reactions occur at the interface between the electrode and electrolyte. Nevertheless, traditional binary ferrites often exhibit poor intrinsic conductivity and limited electrochemical reversibility, resulting in suboptimal rate capability and rapid capacity fading during extended cycling [1,18].

In order to address these problems, a more complex composition in the ferrite structure has been developed as a compelling design tool. Inspired by the principles of medium entropy and high entropy oxides (MEOs/HEOs), this has been reached via the substitution of different metal cations into the ferrite spinel structure. The thermodynamic stabilization of such systems is governed by configurational entropy, which can be expressed as:

$$\Delta S_{config} = -R\sum_{i=1}^{n} x_i \ln x_i \quad \text{— (i)}$$

View Article Online
DOI: 10.1039/D5TA00340G

where R is the gas constant and x_i represents the mole fraction of each component [18,19]. For the present system, the cationic sublattice consists of four divalent metal ions, namely Mn^{2+}, Co^{2+}, Ni^{2+}, and Zn^{2+}. An equimolar distribution of four cations (Mn^{2+}, Co^{2+}, Ni^{2+}, Zn^{2+}), the entropy is calculated as $\Delta S_{config} = R \ln 4$ (~1.386R). According to established classification, systems with $\Delta_{Sconfig}$ between 1R and 1.5R are categorized as medium-entropy materials, while values ≥1.5R correspond to high-entropy systems. Therefore, the present $(MnCoNiZn)Fe_2O_4$ composition can be classified as a medium-entropy spinel ferrite. These materials gain thermodynamic stabilisation by high configurational entropy, resulting in the minimisation of phase segregation and formation of single phase even at moderate temperatures. The simultaneously existent different transition metals also result in several redox active species and synergistic cationic interactions that enhance charge transfer, ionic diffusion and electronic conduction [20,21].

The synergistic effects of the cations are obviously important. The Mn^{2+} ions enhance both ionic and electronic transport and promote reversible redox surface changes between the Mn^{2+}/Mn^{3+} states. Meanwhile, cationic centres that are readily attainable such as Co^{2+}/Co^{3+} and Ni^{2+}/Ni^{3+} redox systems are attained via the cations Co^{2+} and Ni^{2+}. The Zn^{2+} ions show a stabilising structural role by their ability to stabilise the spinel structure and also mitigate the cation drift during cycling, whereas the Fe^{3+} ions show some pseudocapacitive phenomena shown in the Fe^{2+}/Fe^{3+} transitions [22–24]. The existence of these species in the one matrix should therefore give a favourable arrangement, where each cation has its own separate contribution to redox activity, conductivity or spinel integrity, allowing an increase of activity in terms of electrochemical performance of the whole array [15].

Although entropy-stabilized ferrites show great potential, their synthesis via conventional solid-state techniques are challenging, due to high temperature calcination (≥1000°C) for a prolonged period of time resulting in grain coarsening, agglomeration and non-uniformity in cation mixing, and lack of accessibility to electrochemical surface area, and redox reaction [25]. In contrast, wet chemical techniques, particularly sol–gel methods offer many advantages including: high homogeneity at the molecular level, stoichiometry control, and, convenience of accessing nano scale particle systems at reduced temperatures of calcination. It also offers the advantage of incorporating organic or biogenic agents to facilitate control of morphology and porosity, important traits for efficient ion transport [2,14,26].

View Article Online
DOI: 10.1039/D5YA00340G

Many recent works have validated the advantages of ferrite systems with multiple cations in electrochemical energy storage devices. For instance, Ganesh et al. (2024) developed Cu-Zn-Mg ferrite electrode systems with a specific capacitance of 508.25 F/g at 1.75 A/g [27]. Agale et al. (2023) synthesized $Cu_{1-x}Ni_xMnFeO_4$ ferrite and achieved capacitance of 975 F/g at high energy density of 20.8 Wh/kg [28]. Yi Yin et al. (2023) reported entropy stabilized oxide $(FeCoCrMnNi)_3O_4$ with a capacitance of 332.2 F/g at 0.3 A/g in alkaline medium [29]. In continued research, Aparna et al. (2018) have made a systematic study of MFe_2O_4 (M = Fe, Co, Ni, Mn, Cu, Zn) observing a high range of capacitance (from >= 101 to 444.78 F/g, showing profile of cation type effectiveness on electrochemical behaviour [30]. Most recent examples are by Hsu et al. (2025) reporting Bi-doped $NiFe_2O_4$ exhibiting high specific capacitance or 339.16 F/g at 5 mV/s, showing advantages of modifications in composing [30]. Collectively, these studies highlight the importance of cation engineering in enhancing electrochemical performance.

On the other hand, the concept of green synthesis approaches has been emerged, in which the biogenic compounds being used as natural stabilizers, complexing agents or structure-directing templates in the synthesis of materials. These biologically active products have tendencies that are inherently beneficial, such as the ability to complex metal ions, gel formation with defined properties, and residues of carbonised material after processing at elevated temperatures [31–33]. Albumen (egg white) is an environment friendly agent, plays a multifunctional role during the synthesis of the ferrite system. Firstly, the proteinaceous functional groups present in albumen ($–NH_2$, –COOH, –OH) facilitate chelating interactions with metal cations (Mg^{2+}, Co^{2+}, Ni^{2+}, Zn^{2+}, Fe^{3+}), ensuring homogeneous mixing at the molecular level [34]. Secondly, albumen acts as a soft template, guiding the nucleation and growth of nanoparticles and preventing agglomeration, thereby contributing to controlled morphology and porosity. Finally, upon thermal treatment, albumen undergoes decomposition to form in situ carbonaceous species, which can enhance electrical conductivity and structural stability of the final material [35,36].

This is ultimately beneficial in enhancing the electroactive interface called up in the terminology. The synthesis employing albumen as the catalyst agent has been shown to be useful for simple binary oxides such as Fe_2O_3 and ZnO. The procedure has previously been little exploited for the production of compositionally complex, entropy-stabilised spinel ferrites [37–39].

View Article Online
DOI: 10.1039/D5YA00340G

In this work, we report the use of albumen-assisted sol-gel synthesis to yield $[Mn_{0.25}Co_{0.25}Ni_{0.25}Zn_{0.25}]Fe_2O_4$, which is a medium-entropy, spinel ferrite developed to have high electroactive and structurally sound properties for supercapacitor uses. When albumen is selected as the biogenic precursor, it not only leads to uniform cation distributions and particle miniaturisation but also a conductive carbonaceous support is produced on calcining the products further improving charge transport. The combined effect of multiple redox-active cationic participants (Mn, Co, Ni, Fe) and the stabilising effect of Zn is expected to lead to beneficial pseudo-capacitance, improved electrical conductivity and significantly good cycling stability.

The structural and morphological properties of synthesized ferrite [MnCoNiZn]Fe2O4 were investigated through extensive analyses such as X-ray diffraction (XRD), Rietveld refinement, X-ray photoelectron spectroscopy (XPS), and electron microscopy. The electrochemical performance was evaluated to establish the relationship between entropy-driven compositional design and charge storage behaviour. The study demonstrates how a biogenic synthesis technique combined with an entropy-driven compositional design can produce a high-performance, sustainable high-performance electrode materials for next-generation supercapacitors.

2. Experimental section

2.1 Materials

The following reagents were used in the synthesis of $[MnCoNiZn]Fe_2O_4$: ferric nitrate nonahydrate ($Fe(NO_3)_3 \cdot 9H_2O$), manganese nitrate hexahydrate ($Mn(NO_3)_2 \cdot 6H_2O$), cobalt nitrate hexahydrate ($Co(NO_3)_3 \cdot 6H_3O$), nickel nitrate hexahydrate ($Ni(NO_3)_2 \cdot 6H_2O$), and zinc nitrate hexahydrate ($Zn(NO_3)_3 \cdot 6H_2O$). All of analytical grade with 98-99% purity were provided by Sisco Research Laboratories (SRL) Pvt. Ltd., India. Pellets of potassium hydroxide (KOH) were also acquired from SRL. Graphite foil (GF) was obtained from Falconi Industries, Hyderabad, while carbon black and polyvinylidene fluoride (PVDF) were acquired from Alfa Aesar, India. In the experiment, distilled water was used as the solvent. The albumen was extracted from fresh chicken eggs that were gathered from a local farm, which acts as a natural stabilizing and templating agent owing to its inherent capping properties. All the reagents were utilized directly as received, without any further purification.

2.2 Preparation of $[MnCoNiZn]Fe_2O_4$

View Article Online
DOI: 10.1039/D5TA00340G

An amount of 40 mL of egg albumen, freshly extracted from chicken eggs, was mixed with 60 mL of distilled water and stirred vigorously to make it a homogeneous mixture. The stoichiometrically calculated amounts of corresponding raw metal nitrate salts of Fe, Mn, Co, Ni, and Zn were subsequently added into the albumen-water solution, where Mn, Co, Ni, and Zn were maintained in equimolar proportions (1:1:1:1), while Fe was added to satisfy the spinel stoichiometry of $[Mn_{0.25}Co_{0.25}Ni_{0.25}Zn_{0.25}]Fe_2O_4$. The mixture was maintained at a temperature of 70 °C on a hot plate magnetic stirrer with bead rotation at 400 rpm until it transformed into a viscous gel, signifying the completion of gelation. The gel was then dried in an oven at a temperature of 100 °C for a duration of 6 hours to remove the residual moisture content, resulting in a solid like mass. This dried mass was then finely ground with an agate mortar and subjected to calcination at various temperatures - 400 °C, 600 °C, 800 °C, 1000 °C and 1100 °C for 4 hours duration with 3 °C/min of rise and fall temperature in a muffle furnace. To maintain its phase uniformity and regulate particle growth, the material was intermittently ground during each calcination process. The final calcined material appeared as a blackish-brown powder, confirming the successful synthesis of $[Mn_{0.25}Co_{0.25}Ni_{0.25}Zn_{0.25}]Fe_2O_4$. The albumen-assisted final product was designated as MCNZF, representing the composition of $[Mn_{0.25}Co_{0.25}Ni_{0.25}Zn_{0.25}]Fe_2O_4$ obtained by employing this bio-mediated sol-gel route. A schematic representation of the synthesis strategy is provided in Figure 1.

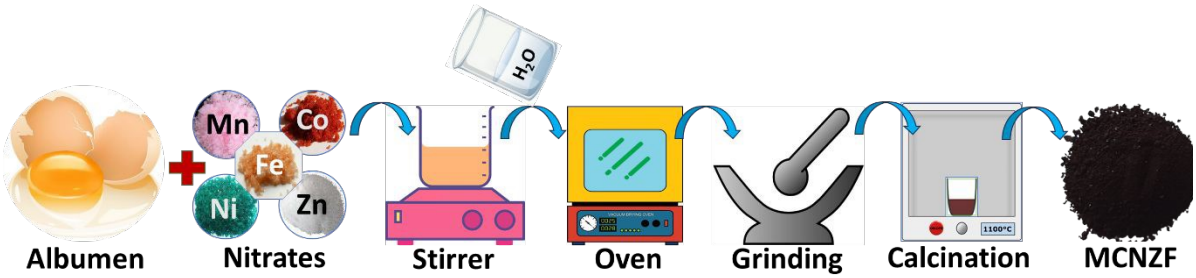

Figure 1. Schematic flow of MCNZF synthesis

2.3 Material Characterization

The synthesized MCNZF spinel ferrite was characterized to analyse its structural, chemical, compositional, morphological, optical, and electrochemical properties. Crystallographic analysis was conducted using X-ray diffraction (XRD) (PANalytical Empyrean diffractometer, Cu Kα radiation (λ = 1.5404 Å), scanning 2θ range of 10° to 80°, step size of 0.020°) to confirm phase purity and determine lattice parameters. Rietveld refinement was performed using the FullProf software tool with ICSD data base, to obtain precise structural information. Raman

View Article Online
DOI: 10.1039/D5YA00340G

spectroscopy was carried out (Horiba Jobin Yvon T64000 triple monochromator, 514 nm Ar+ laser, Backscattering mode) to identify the vibrational modes of spinel ferrites. Surface elemental composition and oxidation states were examined via X-ray photoelectron spectroscopy (XPS) (Kratos AXIS Supra). The morphology and microstructure of the samples were investigated using Field Emission Scanning Electron Microscopy (FESEM, JEOL JSM-7610F) and High-Resolution Transmission Electron Microscopy (HRTEM, FEI Talos F200X) to resolve lattice fringes and confirm crystal structure at the desired scale. The specific surface area of the sample was evaluated using the Brunauer Emmett Teller (BET) theory method based on N_2 adsorption–desorption isotherms recorded at 77 K. The analysis was performed using an Autosorb iQ Station 1 instrument. The pore size distribution was further calculated employing the Barrett Joyner Halenda (BJH) method. Optical properties were measured (using Shimadzu UV-2401 UV-Visible spectrophotometer (UV)) to identify the absorption spectra and bandgap of the material, while Fourier-transform infrared (FTIR) spectroscopy in the 400-4000 cm^{-1} range (PerkinElmer Spectrum 100) was employed to identify metal-oxygen bonding and molecular vibrations. Electrochemical performance was evaluated through cyclic voltammetry (CV) and galvanostatic charge-discharge (GCD) experiments on a ZIVE MP5 multichannel workstation (WonATech Co., Ltd., Korea), with electrochemical impedance spectroscopy (EIS) measurements were performed (Metrohm AutoLAB 302N equipped with NOVA 2.1 software) to assess charge transfer and capacitive behaviour.

2.4 Preparation of Electrode

The working electrode was fabricated by blending the synthesized MCNZF powder as the primary material, carbon black (CB) to enhance the conductivity and polyvinylidene fluoride (PVDF) as a binder, added in a weight ratio of 80:10:10. To this combination, a consistent amount of N-methyl-2-pyrrolidone (NMP) is added to make a homogeneous slurry. The resulting mixture was then uniformly coated on a graphite foil (GF) substrate (3 cm × 1 cm) using doctor blade, with electrode material spreading on effective area of 1 cm^2. The GF used as the current collector has a thickness of ~0.5 mm, while the deposited active material forms a thin coating layer in the range of ~5-20 µm. The loading of the active material was maintained at roughly 1 mg per electrode. After coating, the electrodes were dried in an oven at temperature of 70 °C for 12 hours duration. These MCNZF coated GF electrode (MCNZF/GF) was subsequently used as the working electrode in a three-electrode supercapacitor configuration for electrochemical evaluations.

View Article Online
DOI: 10.1039/D5YA00340G

2.5 Three electrode system (3E)

The MCNZF/GF electrode was integrated into a three-electrode supercapacitor configuration operated at ambient conditions. In this setup, the prepared electrode used as a working electrode, while a platinum wire acted as a counter electrode and an Ag/AgCl (saturated KCl) electrode was used as a reference. The electrolyte used for the configuration was 2M KOH. An illustration of the complete experimental arrangement is displayed in Figure 2.

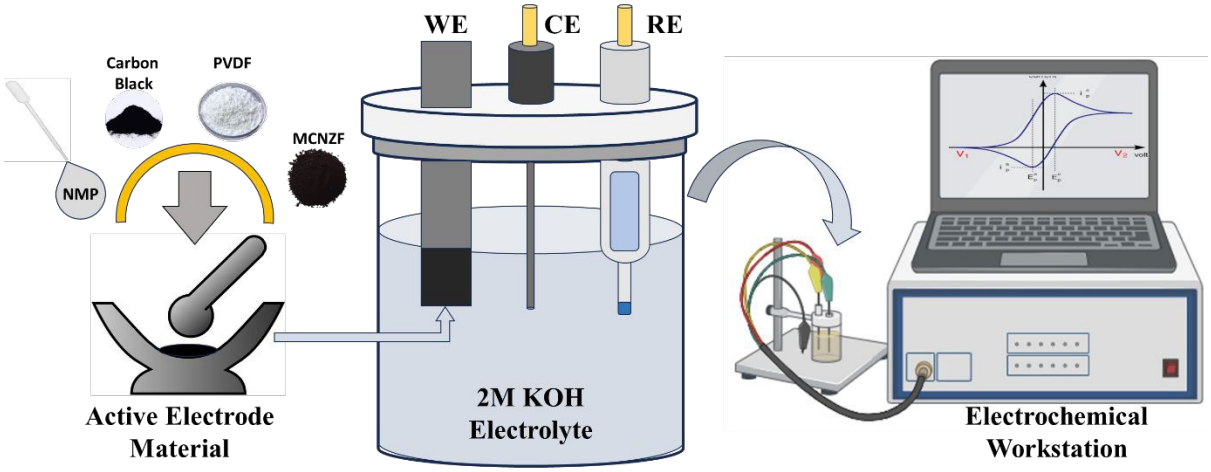

Figure 2. Schematic diagram of three-electrode system (3E)

3. Results and Discussion

Structural Characterization

The structural characterization of the synthesized MCNZF sample was done using XRD analysis, and the corresponding diffraction pattern are shown in Figure 3. The sample was calcined at various temperatures from 400 °C to 1100 °C to determine the optimal condition for achieving well-defined crystalline phases with minimal impurities. The respective XRD patterns were presented in the supplementary information (SI) (Figure S1). At all calcination temperatures, the dominant (major) diffraction peak was appeared at 2θ = 35.60°, corresponding to the principal reflection of Fe_3O_4 structure, confirming the formation of spinel phase (JCPDS No. 65-3107) [14,40,41]. However, at 800 °C, the XRD pattern revealed a minor impurity peak at 2θ = 33.37°, attributed to Fe_2O_3, indicating a partial structural instability. This instability is due to the partial oxidation of Fe^{2+} to Fe^{3+} ions and the redistribution of cations within the spinel lattice [42,43]. In the case of the multicomponent MCNZF sample, which

View Article Online
DOI: 10.1039/D5YA00340G

contains multiple transition metal cations (Mn^{2+}/Mn^{3+}, Co^{2+}/Co^{3+}, Ni^{2+}, Zn^{2+}, and Fe^{2+}/Fe^{3+}), this instability is further influenced by cation migration between tetrahedral (A) and octahedral (B) sites. At intermediate temperatures, the unequal diffusion rates and ionic radii differences among these cations cause local lattice distortion and strain [44–46]. However, with further calcination at higher temperatures, enhanced atomic mobility promotes configurational entropy stabilization, allowing a homogeneous distribution of cations over both sublattices. Upon increasing the calcination temperature to 1000 °C, the impurity peak diminishes significantly, suggesting improved structural ordering. Further heating to 1100 °C results in complete elimination of the impurity, confirming the formation of a single-phase cubic spinel structure with no detectable secondary phases. The diffraction pattern and corresponding Rietveld refinement of the MCNZF sample calcined at 1100 °C, as shown in Figure 3(a), reveal well-defined reflections characteristic of a cubic spinel ferrite structure (space group: *Fd-3m*), closely resembling that of Fe_3O_4. Prominent diffraction peaks observed at $2\theta \approx 18.48°$, 30.26°, 35.60°, 37.25°, 43.24°, 53.61°, 57.12°, and 62.70° correspond to the (111), (022), (113), (222), (004), (224), (115), and (044) planes, respectively, consistent with the ICSD collection code 158745 [47–49]. The Rietveld refinement yielded $R_p = 37.0$, $R_{wp} = 21.2$, and $R_e = 19.1$, with a goodness-of-fit value chi-square (χ^2) ≈ 1.23, indicating a satisfactory agreement between the experimental and calculated diffraction patterns and confirming the formation of a single-phase cubic spinel structure with excellent structural homogeneity and phase purity. The respective Rietveld refinement parameters are shown in the Table S1 in SI.

The Raman spectrum of synthesized MCNZF is shown in the Figure 3(b). The MCNZF sample exhibit characteristic peaks corresponding to the vibrations of the spinel structure. These vibrational modes are related to the stretching and bending of bonds in the spinel lattice, specifically involving the oxygen ions and the metal cations in the tetrahedral (A) and octahedral (B) sites [50]. The Raman-active modes of a spinel structure with *F d -3 m* symmetry are derived from group theory and typically include A_{1g} (Symmetric stretching of the A-site metal-oxygen bonds), E_g (Symmetric stretching vibrations of oxygen atoms), T_{2g} (Various bending and stretching vibrations). For ferrites, these modes generally appear in the following regions for A_{1g} : ~600 - 700 cm^{-1} (strong peak, associated with the tetrahedral A-site metal-oxygen bonds), T_{2g}: ~200 - 500 cm^{-1} (weaker peaks, associated with vibrations of the B-site metal-oxygen bonds). In the synthesized MCNZF strong A_{1g} mode splits into two distinct modes ($A_{1g}(1)$, $A_{1g}(2)$) due to cation inversion in the spinel structure, around at 683 cm^{-1} and 613 cm^{-1} corresponding to the Fe-O bond vibrations. The multiple T_{2g} modes ($T_{2g}(1)$, $T_{2g}(2)$,

View Article Online
DOI: 10.1039/D5TA00340G

$T_{2g}(3)$ are at 475 cm^{-1}, 373 cm^{-1} and 182 cm^{-1}, reflecting the interactions, due to Mn, Co, Ni, and Zn ions. The shift of $T_{2g}(3)$ below 200 cm^{-1} is due to the influence of Co and Zn. The E_g mode is appeared at 321 cm^{-1} [2,40]. The factors influencing Raman peaks are cation distribution of Mn, Co, Ni, Zn, and Fe between the tetrahedral and octahedral sites affects peak positions and intensities. The broadening of peaks is due to the increased disorder by entropy effects from multiple cations. The particle size and synthesis approach may also effect the shifting or broadening of peaks due to strain, defects, or quantum confinement [6,41]. The presence of residual carbon is identified in Raman and displayed in Figure S2(a)

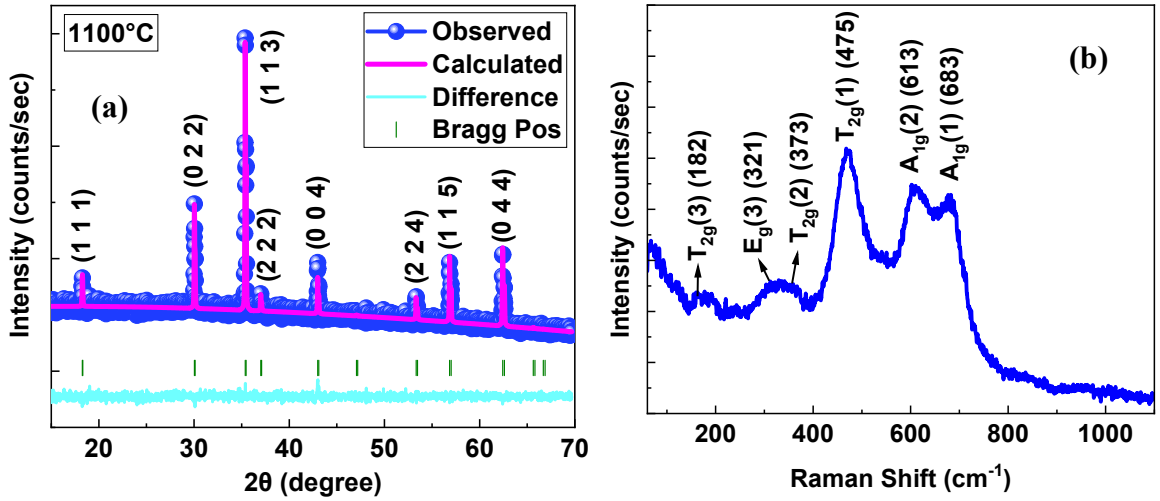

Figure 3. (a) XRD and Rietveld fit (b) Raman spectra of MCNZF

The XPS was employed to identify the elemental composition and oxidation states of the synthesized MCNZF sample. The corresponding spectra are displayed in Figure 4, including both the wide survey scan spectra and high-resolution core-level spectra for elements Mn, Co, Ni, Zn, Fe, C, and O. The survey spectrum (Figure 4a) confirms the presence of all the elements in the synthesized MCNZF material, while the specific deep scans provide detailed insights into their chemical states. In Figure 4b, the Mn 2p spectrum shows peaks at 640.2 eV (Mn $2p_{3/2}$) and 651.7 eV (Mn $2p_{1/2}$), which deconvolutes into components corresponding to Mn^{3+} and Mn^{2+} oxidation states. The Co 2p spectrum (in Figure 4c) displays two main peaks at 780.4 eV and 794.3 eV, along with two satellite peaks at 785.8 eV and 802.4 eV respectively, confirming the coexistence of Co^{3+} and Co^{2+} oxidation states. In Figure 4d, the Ni 2p peaks observed at 854.1 eV ($2p_{3/2}$) and 872.2 eV ($2p_{1/2}$), accompanied by a satellite peak at 860.1 eV, indicating the exclusive presence of Ni^{2+} in the sample. The Zn 2p spectrum (Figure 4e) shows peaks at 1019.6 eV and 1042.2 eV, characteristic of Zn^{2+}. The Fe 2p

View Article Online
DOI: 10.1039/D5TA00340G

spectrum (Figure 4f) exhibits peaks at 709.9 eV and 723.3 eV, along with satellite peak features at 717.6 eV and 731.8 eV, confirming the coexistence of Fe^{3+} and Fe^{2+} oxidation states [21,27,51,52]. The O 1s spectrum (Figure 4g) presents a dominant peak at 529.6 eV, corresponding to lattice oxygen (metal-oxygen bonds), with additional components attributed to C=O, Fe-O-C, and Fe-O-Fe linkages. The C 1s spectrum (Figure 4h) shows a primary peak at 284.6 eV, assigned to C-C, C-O, and O-C=O functional groups, indicating the presence of residual surface carbon species [1,53]. Overall, the XPS results confirm the successful incorporation of Mn, Co, Ni, Zn, and Fe into the spinel lattice, with mixed valence states that are crucial for the conductivity and electrochemical behaviour of the MCNZF spinel ferrite.

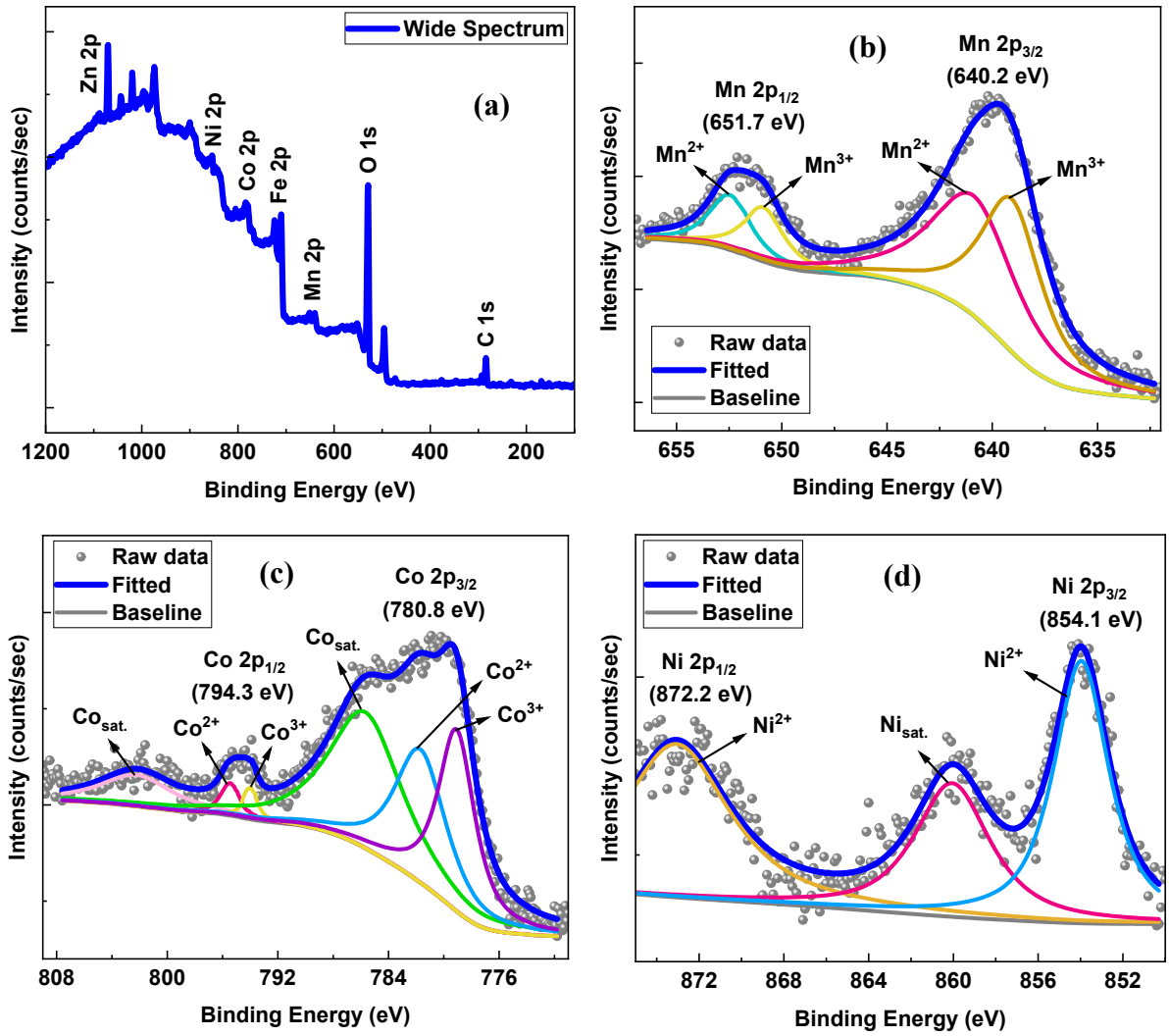

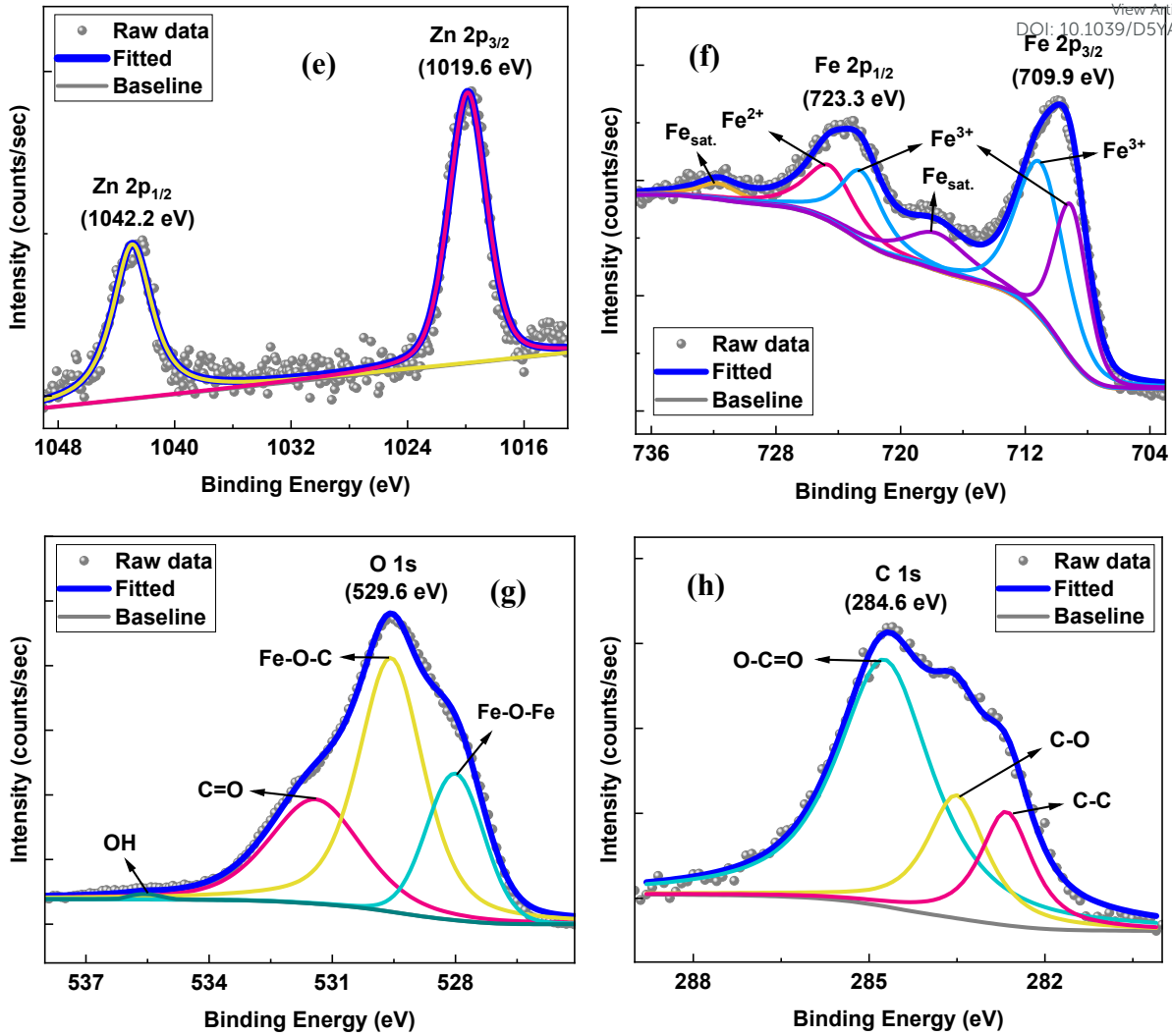

Figure 4. (a) Wide Survey Spectrum (b) Mn 2p (c) Co 2p (d) Ni 2p (e) Zn 2p (f) Fe 2p (g) O 1s (h) C 1s

Morphology Characterization

The surface morphology of the synthesized MCNZF sample was investigated using FESEM, as displayed in Figure 5(a). The micrograph of the MCNZF calcined at 1100 °C reveals well-defined crystalline particles with particles ranging from 200 nm to 2 µm. Additional FESEM images captured at various magnifications are provided in Figure S2 of SI, which further confirm the uniform surface texture and distribution of particles. The increase in calcination temperature facilitates grain growth and densification, resulting in larger particle dimensions due to enhanced diffusion and coalescence processes [54,55]. The morphology displays a predominantly polygonal structure with sharp-edged grains, and in some regions, pyramidal-shaped crystallites are observed, suggesting the presence of anisotropic growth

facets during thermal treatment. Notably, no significant evidence of agglomeration is detected, indicating effective stabilization of the particles during synthesis, likely due to the albumen-assisted route that prevented uncontrolled particle clustering. The Energy-Dispersive X-ray (EDX) spectrum, presented in Figure 5(b), confirms the presence of all constituent elements - Mn, Co, Ni, Zn, Fe, and O, corresponding to the stoichiometric formula of the MCNZF composition. The elemental distribution, as depicted in the EDX elemental mapping (Figure 5(c)), demonstrates a homogeneous dispersion of metal cations throughout the sample without any phase segregation. This uniformity in elemental distribution suggests successful incorporation of all transition metals into the spinel lattice, reinforcing the compositional stability and purity of the synthesized medium-entropy spinel ferrite. The albumen-derived carbon residue is shown in the magnified EDX image in Figure S2(b) of SI.

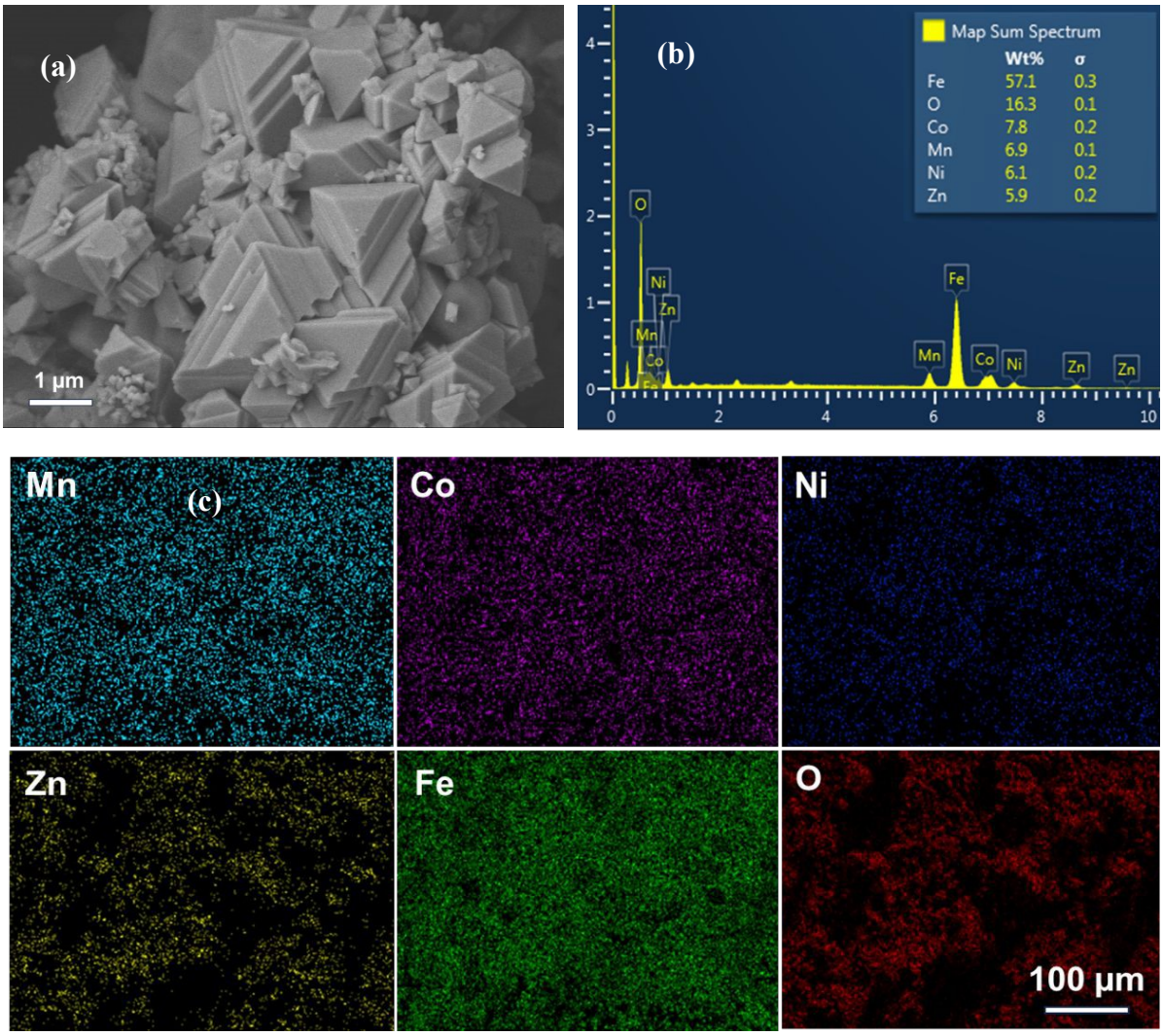

Figure 5. (a) FESEM images (b) EDX (c) Elemental mapping

View Article Online
DOI: 10.1039/D5TA00340G

The HRTEM analysis was carried out on the synthesized MCNZF sample calcined at 1100 °C to gain deeper insights into its microstructural properties, as shown in Figure 6(a) and 6(b). The micrographs display irregular, non-spherical particles with sizes ranging from a few hundred nanometres to several micrometres, suggesting the formation of well-crystallized grains at elevated temperature. The SAED pattern shown in Figure 6(c) exhibits distinct concentric diffraction rings, which can be indexed to the (022), (113), (004), (115), and (044) planes. These reflections are in good agreement with the XRD results, confirming the polycrystalline nature of the spinel MCNZF material. The lattice-resolved HRTEM image in Figure 6(d) reveals clear and well-defined lattice fringes with interplanar spacings of 0.239 nm and 0.253 nm, corresponding to the (222) and (113) planes, respectively. These values are consistent with the XRD analysis, further validating the formation of the spinel structure and crystalline phase formation. The HAADF-STEM images and elemental mapping (Figure 6(e)) reveal a uniform spatial distribution of Mn, Co, Ni, Zn, Fe, and O, indicating successful incorporation of the constituent cations within the spinel lattice and the absence of phase segregation, characteristic of a homogeneous medium-entropy ferrite structure.

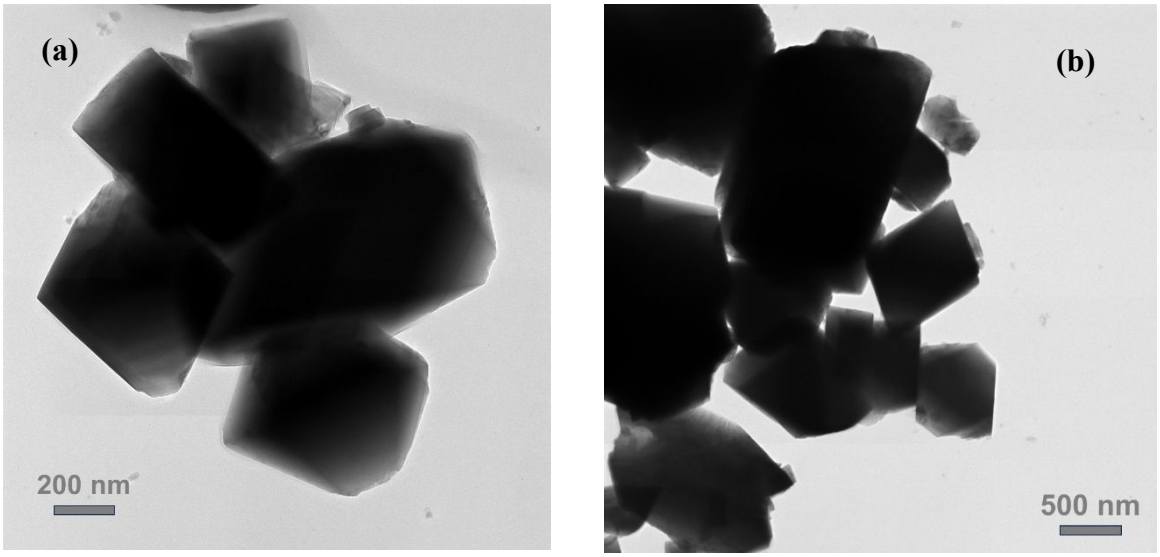

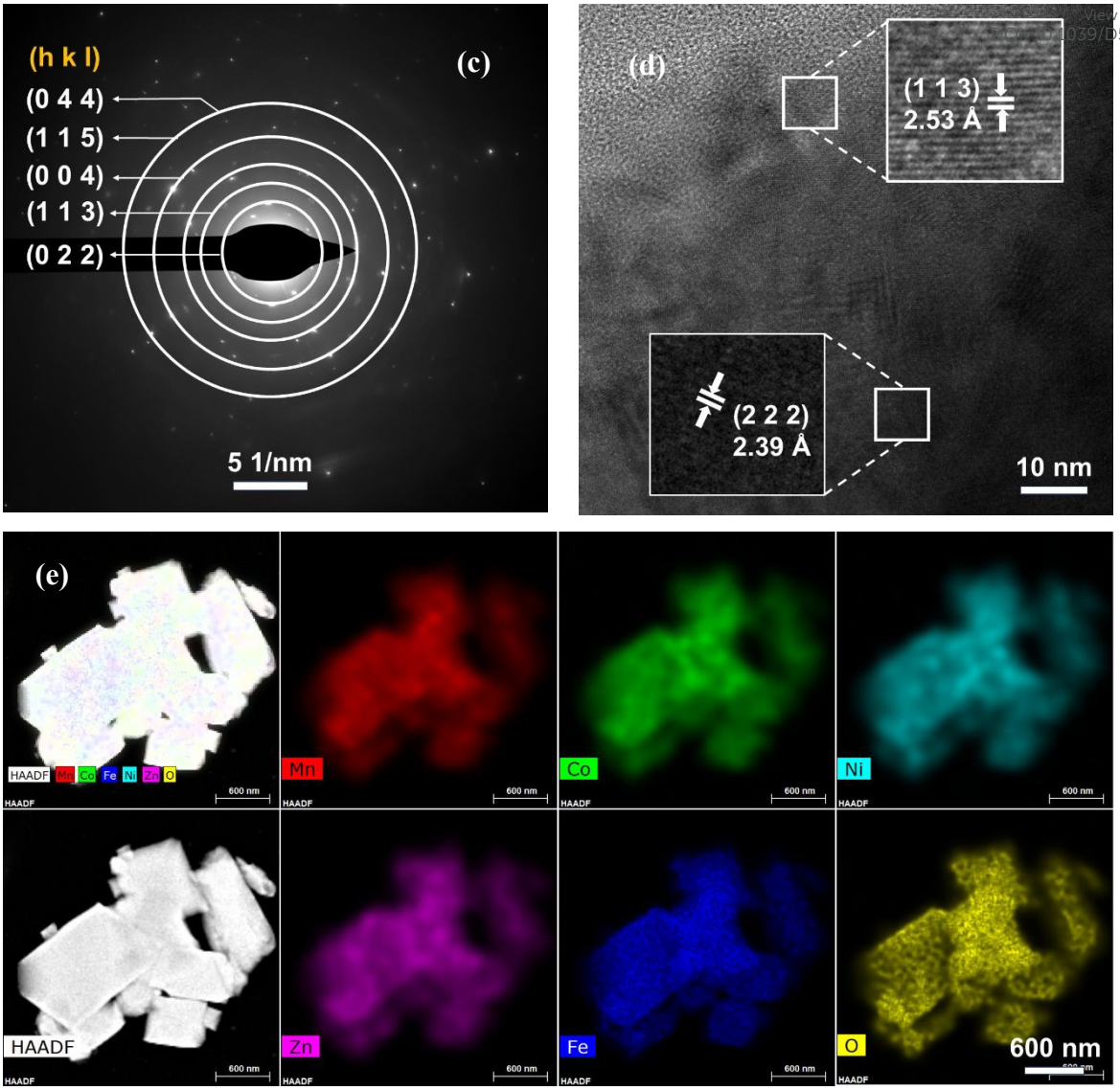

Figure 6 (a) HR-TEM image at 200 nm (b) HR-TEM image at 500 nm (c) SAED Pattern (d) Lattice Spacing images (e) HAADF-STEM image

338

339 ***Textural Characterization***

340 To investigate the textural characteristics of the material, nitrogen (N_2) adsorption-desorption
341 measurements were performed to estimate the specific surface area, pore size distribution, and
342 pore volume. The obtained adsorption-desorption isotherm (relative pressure versus adsorbed
343 quantity), along with the BJH pore size distribution curve (pore diameter versus pore volume)
344 and the corresponding BET plot (inset), are provided in Figure 7(a) and 7(b). The isotherm
345 exhibits a typical Type IV profile with an H3 hysteresis loop, indicating the presence of
346 mesoporous structures [56]. The absence of a limiting adsorption at high relative pressure
347 suggests slit-shaped pores formed by the aggregation of particles rather than well-defined

View Article Online
DOI: 10.1039/D5YA00340G

cylindrical pores [34]. Such a pore structure arises from interparticle voids and results in a non-uniform pore network. The calculated BET surface area of the sample is 4.161 m^2/g, accompanied by a total pore volume of 0.0086 cm^3/g. The average pore radius is determined to be 4.12 nm, further confirming the mesoporous nature of the material. Despite the relatively low surface area, the presence of mesopores suggests a moderately porous framework with accessible channels that can support efficient ion diffusion. This textural feature supports diffusion-dominated charge storage behaviour, consistent with the low surface area and high diffusion-controlled contribution observed in electrochemical analysis.

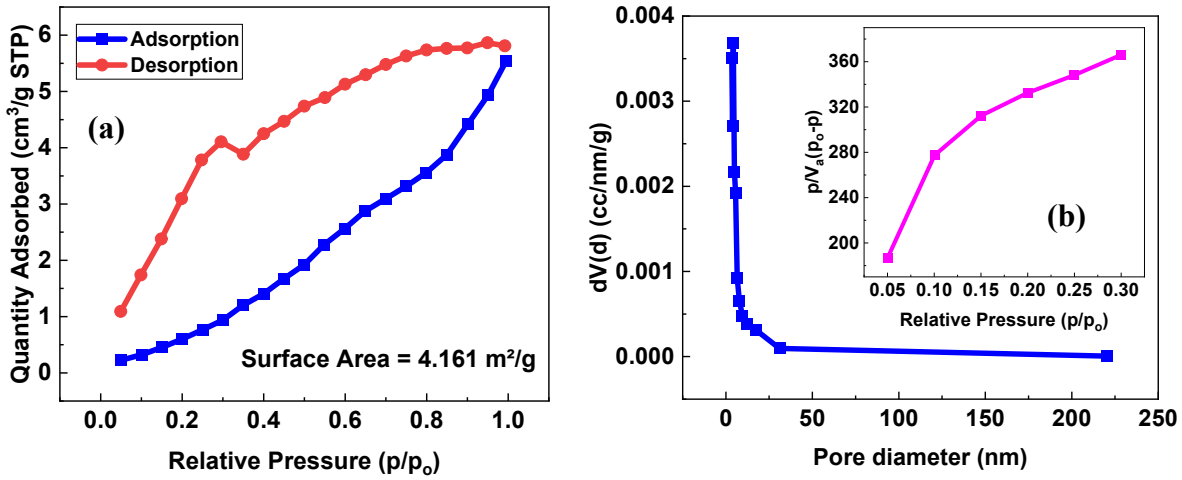

Figure 7. (a) N_2 adsorption-desorption isotherm (b) BJH plot and BET plot (Inset)

Optical Characterization

The FT-IR spectroscopy was performed to identify the functional groups present in the MCNZF composition in the range of wavenumber 400-4000 cm^{-1}. The recorded spectrum, displayed in Figure 8(a), shows the distinct absorption bands observed at 578, 1103, 1631, and 3436 cm^{-1}. The strong band observed at 578 cm^{-1} is due to the metal-oxygen (M-O) stretching vibrations, corresponding to the cations occupying tetrahedral and octahedral sites in the spinel lattice. The band observed at 1103 cm^{-1} is due to the C-OH stretching vibration, while the peak around 1631 cm^{-1} is related to C-O bending vibrations. The broad band near 3436 cm^{-1} corresponds to O-H stretching vibrations, arising from adsorbed or coordinated water molecules [14,57,58]. These spectral features collectively confirm the formation of a pure spinel phase, with no evidence of amides related to albumen remains.

The optical behaviour of the synthesized MCNZF sample was analyzed using UV-Visible spectroscopy over the wavelength ranging from 200-800 nm (displayed in Figure S3

View Article Online
DOI: 10.1039/D5TA00340G

of SI) to gain insights into its electronic structure and optical transition mechanisms. The obtained absorption spectrum exhibited a distinct absorption edge in the visible region, indicating the semiconducting nature of the material. The optical band gap energy was evaluated using Tauc's relation which correlates the absorption coefficient (α) and the incident photon energy (hν) [59–61]. For the MCNZF sample, the plot of $(\alpha h\nu)^{1/2}$ vs hν was constructed, as shown in Figure 8(b), suggesting an indirect allowed transition mechanism. The linear portion of the plot was extrapolated to intersect the energy axis at $(\alpha h\nu)^{1/2} = 0$. The calculated optical band gap energy using equation E1 (in SI) is of 2.86 eV. The calculated band gap value reflects a moderate electronic separation between the conduction band and valence band, confirming the semiconducting nature of MCNZF sample. This intermediate band gap lies within the visible region, which makes effective absorption energy conversion applications. Furthermore, the observed optical response suggests possible charge transfer transitions between the metal cations, contributing to the absorption in the visible range. Such transitions are beneficial for electronic conductivity and surface reactivity, both crucial for electrochemical properties [62,63].

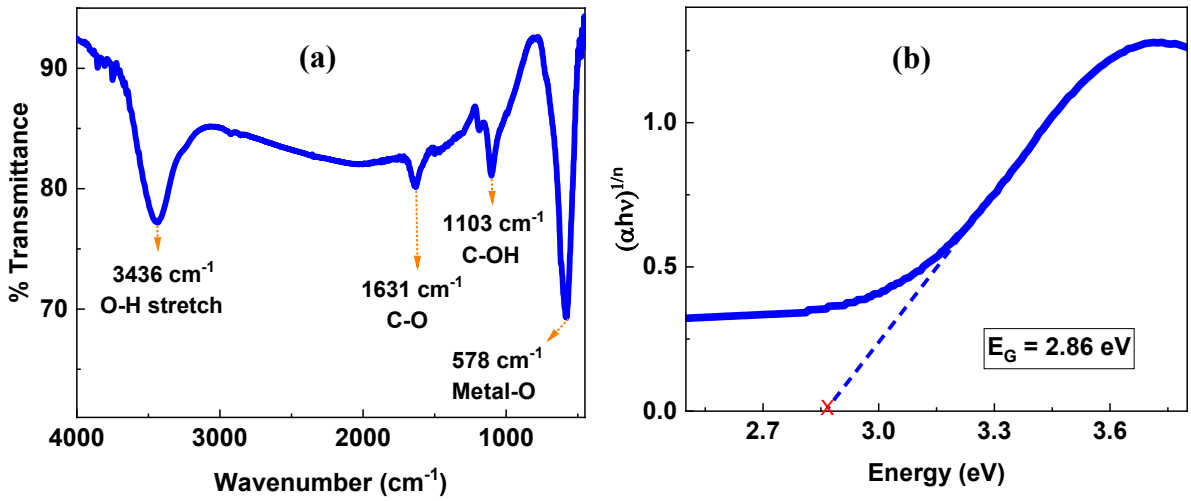

Figure 8. (a) FTIR (b) Tauc plot

Electrochemical Performance

The electrochemical performance of the synthesized MCNZF sample was evaluated using a three-electrode configuration in an electrolyte of 2M KOH. Cyclic voltammetry (CV), galvanostatic charge-discharge (GCD), and electrochemical impedance spectroscopy (EIS) measurements were performed to investigate the capacitive behaviour and charge transfer characteristics of the electrode material.

View Article Online
DOI: 10.1039/D5YA00340G

Cyclic voltammetry study

CV was performed on the fabricated MCNZF/GF electrode in a potential window range of -1.4 V to -0.4 V at a different scan rate varying from 5 mV/s to 200 mV/s, as illustrated in Figure 9(a). The CV curves exhibited a progressive increase in the area of the enclosed loop and also in corresponding current response with increasing scan rate, which indicating the enhanced charge storage kinetics and improved ion diffusion at a higher sweep rate. This trend reflects the good rate of capability and electrochemical reversibility of the MCNZF/GF electrode. A comparison of the MCNZF/GF electrode with the bare GF electrode is presented in Figure S5(a) of SI, confirming the enhanced electrochemical activity upon MCNZF coating.

The CV profile at a scan rate of 5 mV/s (Figure S5(b) of SI) exhibits well-defined redox peaks, with an anodic (oxidation) peak around -0.84 V and a cathodic (reduction) peak around -1.12 V. These distinct peaks indicate the pseudocapacitive nature of the material, originating from Faradaic redox reactions involving multiple valence states of the transition metal ions (Fe^{3+}/Fe^{2+}, Mn^{3+}/Mn^{2+}, Co^{3+}/Co^{2+}, and Ni^{2+}, Zn^{2+}) which are identified from XPS. The coexistence of divalent and trivalent cations enables rapid and reversible electron transfer, contributing to high capacitive performance through surface process or near-surface redox processes [64].

To quantitatively distinguish between the capacitive and diffusion-controlled charge storage mechanism, the scan rate-dependent CV data were analyzed using Dunn's method [65]. In this approach, the total current at a selected potential (V) and scan rate (v) is expressed as a linear combination of capacitive and diffusion-controlled contributions:

$$i(V,v) = k_1(V)v + k_2(V)v^{1/2} \qquad (1)$$

Here, $k_1(V)v$ represents the surface-controlled (capacitive or electrochemical double-layer capacitance (EDL)-type) current, while $k_2(V)v^{1/2}$ corresponds to the diffusion-controlled (pseudocapacitive) current. Rearranging the equation yields:

$$i(V,v)/v^{1/2} = k_1(V)v^{1/2} + k_2(V) \qquad (2)$$

By plotting $i(V,v)/v^{1/2}$ versus $v^{1/2}$ at selected potentials across different scan rates (5, 10, 20, and 50 mV/s), as shown in Figure 9(b), the parameters k_1 and k_2 were extracted to evaluate the quantitative contributions of the capacitive and diffusion-controlled processes. The Dunn analysis was conducted in the potential window of -1.4 to -0.4 V. The analysis was restricted

View Article Online
DOI: 10.1039/D5TA00340G

to moderate scan rates to avoid deviations arising from polarization and diffusion limitations at higher scan rates, ensuring reliable interpretation of charge storage contributions.

At 5 mV/s, the pseudocapacitive contribution accounted for 84.85% of the total current, while the capacitive (EDL) contribution was 15.16%. The respective capacitive and diffusion-controlled regions derived from the CV curve at 5 mV/s are illustrated in Figure 9(d). The relatively smaller capacitive region suggests that charge storage in MCNZF/GF is predominantly governed by diffusion-controlled Faradaic processes rather than purely EDL behaviour [20,41,66]. As the scan rate increases, the capacitive fraction gradually rises due to faster surface-limited processes, as shown in the bar graph in Figure 9(c). The variation of pseudocapacitive and EDL contributions with scan rate is depicted in Figure S5(c) of SI, where the pseudocapacitive and EDL fractions were 63.10% and 36.10% respectively at 50 mV/s. This confirms the synergistic coexistence of EDL capacitance and Faradaic reactions governing the overall charge storage behaviour of the MCNZF/GF electrode.

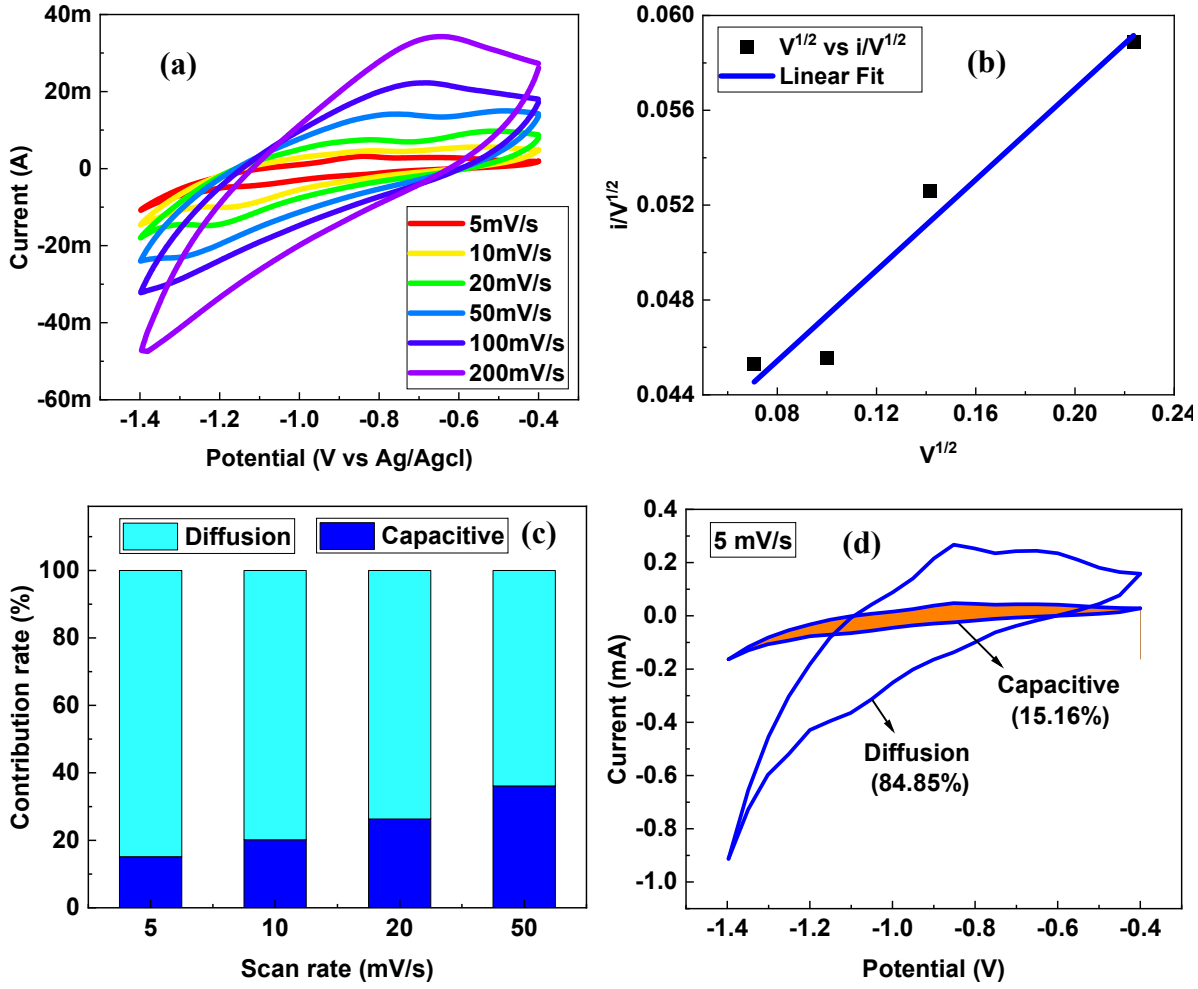

View Article Online
DOI: 10.1039/D5YA00340G

Figure 9. (a) Cyclic voltammetry at various scan rates (b) Linear fit for selected scan rates (c) Capacitance contribution % (d) Capacitive and diffusion-controlled regions at 5mV/s

Galvanostatic charge-discharge test (GCD) study

The charge storage behaviour of the MCNZF/GF electrode was further examined by GCD analysis within the potential range of -1.2 V to -0.4 V at varying current densities of 4, 8, 12, and 16 A/g, as illustrated in 9(a). The high current density range (up to 16 A/g) was used to probe the ability of the electrode to sustain rapid charge-discharge processes under stringent conditions. The GCD curves display nearly symmetrical triangular shapes with minor deviations resembling plateaus, particularly at lower current densities. Such features are indicative of a hybrid charge storage mechanism involving both EDL and pseudocapacitive contributions [15,51,66,67]. The small plateau-like regions appearing within the potential range of -1.2 to -0.8 V in Figure 10(a), most are at a current density of 4 A/g, can be attributed to Faradaic redox reactions involving transition metal ions, which operate in conjunction with the non-Faradaic double-layer charging process. This observation confirms that the MCNZF/GF electrode exhibits a combined EDL and pseudocapacitive behaviour, consistent with the CV and Dunn method analyses. Based on these results, a current density of 4 A/g was selected for long-term GCD cycling, and performed 1500 cycles with selected cycle numbers are presented in Figure S5(d) of SI. The electrode achieved a maximum specific capacitance of 408.18 F/g at 4 A/g calculated using equation (2) shown in SI, which gradually decreased with increasing current density due to reduced ion diffusion efficiency and limited active material utilization at higher charge-discharge rates. The dependence of specific capacitance (C_{sp}) on current density is plotted in Figure 10(b), and the corresponding numerical values are summarized in Table 1.

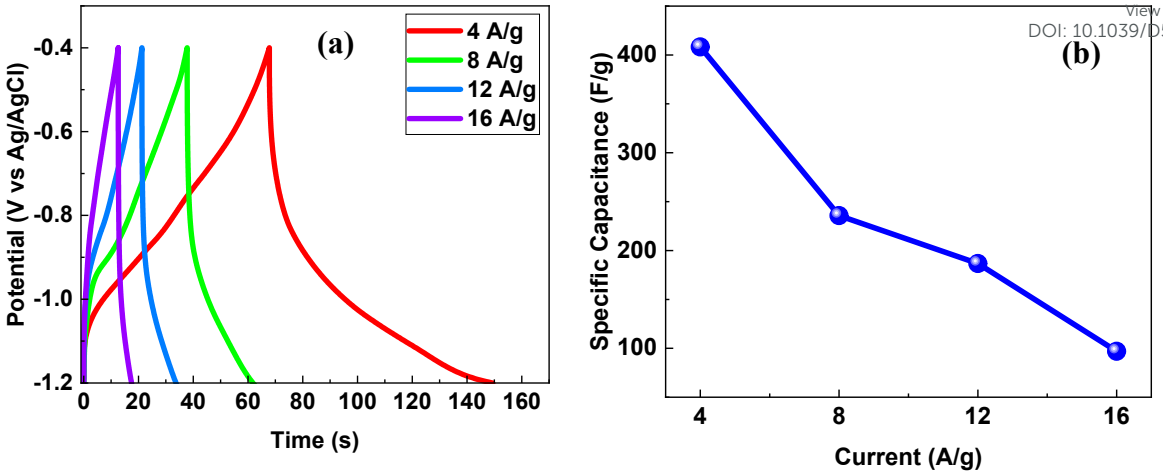

Figure 10. (a) GCD at various current densities (b) Variation of C_{sp} w.r.t current density

Table 1. Variation of C_{sp} with current density and cycle number

Current density (A/g)	C_{sp} (F/g)	Cycle Number	C_{sp} (F/g)
4	408.18	**1**	408.18
8	235.74	**500**	293.305
12	186.75	**1000**	288.085
16	97	**1500**	285.695

Cyclic Stability

The long-term cycling stability of the MCNZF/GF electrode was performed through GCD measurements at a selected current density of 4 A/g for 1500 continuous cycles. The variation of specific capacitance (C_{sp}) with the cycle number is depicted in Figure 11(a), and the corresponding data are summarized in Table 1. As shown in Figure 11(b), the coulombic efficiency remained relatively stable with minimal degradation throughout the cycling process but capacitance retention is moderately stable. After 1500 cycles performance, the electrode preserved 66.79% of its initial specific capacitance, indicating good structural robustness and electrochemical reversibility during repeated charge-discharge operations. Moreover, a high coulombic efficiency of 91.55% was maintained, suggesting efficient charge-discharge kinetics and excellent energy recovery during prolonged cycling [53,68]. The moderate capacitance retention observed can be primarily attributed to the bulk nature and also due to the changes induced during repeated ion insertion/extraction processes, rather than solely to the bulk nature of the MCNZF material. In bulk electrodes, ion transport and electrolyte

penetration are often restricted to the surface or near-surface regions, resulting in limited utilization of the inner active sites during cycling. Over prolonged charge-discharge operation, the repetitive volume expansion and contraction associated with Faradaic redox reactions may induce mechanical stress, partial cracking, and also loss of electrical contact between active particles with the current collector. These effects collectively contribute to gradual performance fading [3,69,70]. Nevertheless, the high coulombic efficiency confirms that the charge storage process remains largely reversible, demonstrating stable electrochemical kinetics despite structural limitations inherent to bulk materials. It is important to note that the reported electrochemical values are derived from a 3E configuration and reflect the intrinsic behaviour of the material. Due to the narrow potential window of ferrite-based electrodes in symmetric systems, these materials are more effectively utilized in asymmetric configurations to achieve enhanced operating voltage and energy density.

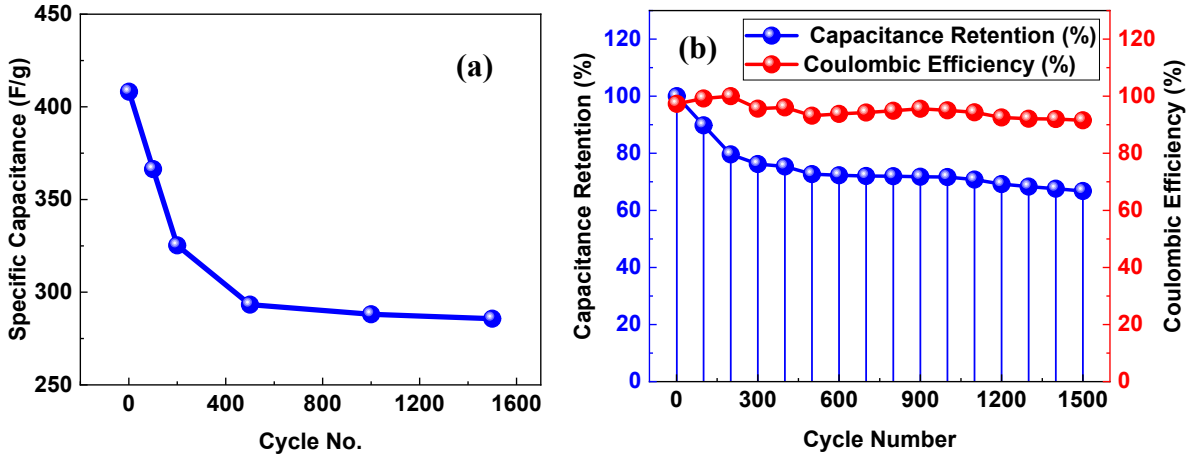

Figure 11. (a) Variation of C_{sp} w.r.t cycle number (b) Capacitance retention and coulombic efficiency

Electrochemical Impedance Spectroscopy (EIS)

EIS was performed to examine the intrinsic resistance and charge-transfer behaviour of the MCNZF/GF electrode [14,27,70]. The measurements were carried out in 2 M KOH electrolyte over a frequency range of 0.1 Hz-100 kHz with an AC amplitude of 5 mV at open-circuit potential. The Nyquist plot presented in Figure 12(a), together with the equivalent circuit shown in the inset, was analyzed using a modified Randles-type model. The Bode plots (phase angle vs frequency) before and after GCD were presented in Figure S6(a), S6(b) of SI. In the high-frequency region, a small semicircular arc is observed, corresponding to the charge-transfer resistance (R_{ct}) at the electrode-electrolyte interface. For the new electrode, the low

View Article Online
DOI: 10.1039/D5TA00340G

semicircle diameter indicates a small R_{ct} of approx. 24.91 Ω, implying efficient redox kinetics and facile charge transport through the bulk structure. After performing GCD cycling, the semicircle got expands, yielding an increased R_{ct} value of about 38.75 Ω. The other parameters were included in Table S2 in SI. This rise can be attributed due to the formation of resistive surface films, microstructural rearrangements, and partial blockage of electroactive sites within the bulk matrix, leading to the diminished ion-diffusion and decreased electron conduction pathways. Consequently, the overall conductivity and specific capacitance decrease upon prolonged cycling. The favourable impedance response of MCNZF/GF mainly arises from the synergistic role of multiple transition metals such as Co, Ni, and Fe, which provide abundant redox-active centres and enhance electronic conductivity [3,24,40]. Meanwhile, Mn and Zn contribute primarily to structural stability and lattice uniformity, minimizing the mechanical degradation during cycling.

Ragone Plot

The Ragone plot of the MCNZF/GF was constructed to evaluate and compare the energy and power density characteristics, as shown in Figure 12(b). The energy density (E) and power density (P) were calculated using Equations (E4) and (E5) of SI, respectively. The MCNZF/GF exhibited a maximum energy density of 36.31 W h/kg at a corresponding power density of 1601.28 W/kg at a current density of 4 A/g. The energy and power densities are calculated based on a 3E configuration and represent electrode-level performance. These results are comparable to or exceed previously reported values for other high-performance transition metal-based spinel and entropy-stabilized supercapacitor electrodes [6,11,25]. Upon increasing the current density up to 16 A/g, the MCNZF/GF electrode still maintained an energy density of 8.63 W h/kg at a high-power density of 6405.12 W/kg, demonstrating significantly good rate capability and fast charge-discharge kinetics. The superior energy power performance of the MCNZF/GF electrode can be attributed to its highly crystalline spinel structure, rich redox-active sites due to multiple transition metals, and the synergistic effect of entropy stabilization, which promotes enhanced charge storage behaviour. These electrochemical characteristics alongside the high specific capacitance, long-term cycling durability and robust structural integrity highlight the potential of MCNZF as a promising electrode material for advanced energy storage applications.

Collectively, the EIS, CV, and GCD analyses reveal that the MCNZF/GF electrode exhibits low interfacial resistance, acceptable ion transport, and moderately stable

View Article Online
DOI: 10.1039/D5EA00340G

electrochemical behaviour, demonstrating its potential for hybrid or pseudocapacitive energy storage applications.

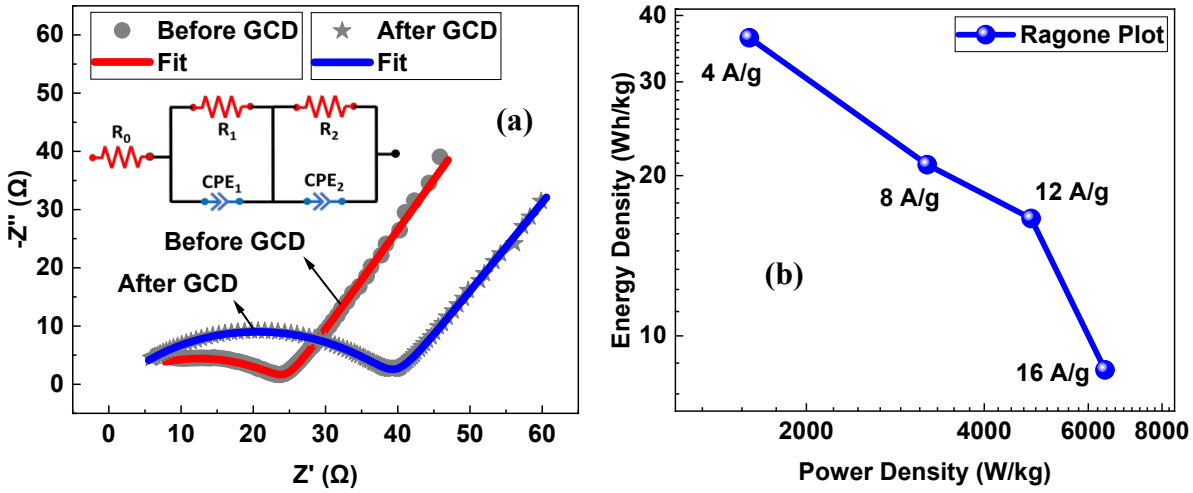

Figure 12. (a) Nyquist plot of MCNZF/GF before and after GCD (b) Ragone plot

To examine the morphological changes before and after cycling, SEM analysis was carried out. The SEM images of MCNZF/GF before GCD and after GCD with their surface roughness plots are displayed in the Figure 13. The surface roughness analysis derived from profile data reveals a noticeable increase after electrochemical cycling, with the average roughness (R_a) rising from 34.61 to 41.18 and the root mean square roughness (R_q) increasing from 43.08 to 48.24. This enhancement in roughness indicates the development of a more uneven and textured surface, which can be attributed to repeated ion insertion/extraction and associated structural rearrangements during cycling [71]. Such changes are consistent with the SEM observations, where the electrode surface becomes comparatively rough without the formation of visible cracks, suggesting mechanical stability of the material. The increased roughness may initially provide additional active sites; however, excessive surface irregularities can also hinder effective electron transport and ion diffusion pathways, contributing to the observed decrease in capacitance upon prolonged cycling [72].

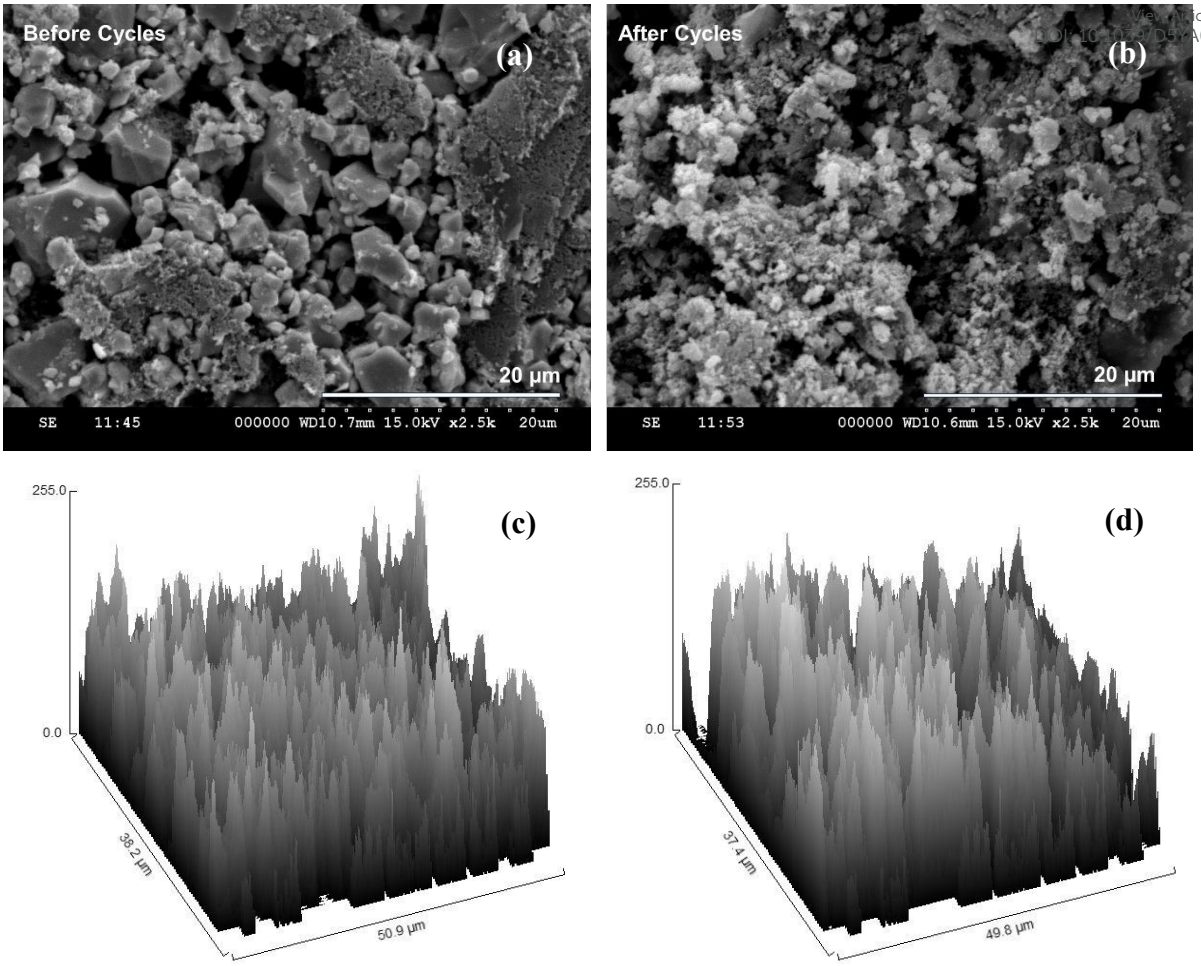

Figure 13. (a) SEM image of MCNZF/GF before GCD (b) SEM image of MCNZF/GF after GCD (c) Surface roughness plot before GCD (d) Surface roughness plot after GCD

The comparison of various synthesis techniques for binary, ternary, and quaternary (entropy) spinel ferrite compounds - along with the different electrolytes, potential windows, current densities and the corresponding specific capacitances reported earlier for supercapacitor applications is presented in Table 2.

Table 2. Comparative summary of recent reports:

Material	Method	Electrode Mass load (mg)	Electrolyte	I (A/g)	PW (V)	C_{sp} (F/g)	Stability @cycles	Ref.

$[NiCo]Fe_2O_4$	Sol-gel	-	1M KOH	1	-1 to 1	50.0	20% @200	[73]
$[NiCu]Fe_2O_4$	Sol-gel	-	1M KOH	1	-1 to 1	44.0	5% @200	[73]
$[CuCo]Fe_2O_4$	Sol-gel	-	1M KOH	1	-1 to 1	76.9	80% @200	[73]
$[CuCo]Fe_2O_4$	Sol-gel	~1	1M KOH	1		397.0	50% @300	[74]
$[CoMg]Fe_2O_4$	Sol-gel combustion	~1	2M KOH	0.5	0 to 0.4	579.3	96.49% @1000	[75]
$[AlxCuyCo_z]Fe_2O_4$ (x+y+z=1)	Sol-gel	-	1M KOH	2	-1 to 1	256-540	88% @300	[74]
$NiFe_2O_4$/CF	Hydrothermal	-	3M KOH	1	0 to 0.6	490.0	91.3% @5000	[76]
$[ZnMg]Fe_2O_4$	Sol-gel citrate	~1	1M Na_2SO_4	1	0 to 0.4	484.6	-	[77]
$[ZnMgCu]Fe_2O_4$	Solvothermal reflux	~1	1M KOH	1.75	0 to 0.6	508.25	-	[27]
$[CaZnMg]Fe_2O_4$	Solvothermal reflux	-	2M KOH	0.5	0 to 0.6	66.8	-	[78]
$[MnCoNiZn]Fe_2O_4$	Sol-gel	~1	2M KOH	4	-1.2 to -0.4	408.18	66.79% @1500	This work

View Article Online
DOI: 10.1039/D5YA00340G

4. Conclusion

A medium-entropy spinel ferrite [MnCoNiZn]Fe_2O_4 was synthesized via a sol-gel route, forming a cubic spinel single phase with pyramidal shaped particles (200 nm-2 μm). The optical properties of material shown a semiconductive nature with optical band gap of 2.86 eV. Electrochemical analyses revealed a hybrid charge-storage mechanism combining both pseudocapacitive and electric double-layer behaviour, confirmed by Dunn's method. The electrode delivered a significantly high specific capacitance of ~408 F/g at 4 A/g current density, retaining 66.79% of its initial capacitance after 1500 cycles with 91.55% coulombic efficiency. EIS results showed low equivalent series and charge transfer resistance, indicating efficient ion transport and good electrical conductivity. The performance enhancement arises from the synergistic interaction among Fe, Co, and Ni redox-active centres and the structural stability provided by Mn and Zn. Being a bulk material, the limited surface area and longer ion diffusion pathways contribute to moderate cycling stability. Incorporation of graphene oxide or reduced graphene oxide could improve conductivity, surface reactivity, and durability, making [MnCoNiZn]Fe_2O_4 a promising candidate for hybrid supercapacitor applications.

Acknowledgements

The authors gratefully acknowledge the financial support from the Science and Engineering Research Board (SERB), Government of India, by a grant No: CRG/2019/001574. Authors would like to acknowledge the support offered by CSIR-Indian Institute of Chemical Technology. Additionally, the author gratefully acknowledges the University Grants Commission (UGC), India, for financial assistance through the National Fellowship for Other Backward Classes (NFOBC) during the course of this research.

References

[1] A. Manohar, V. Vijayakanth, S. V. Prabhakar Vattikuti, K.H. Kim, Electrochemical investigation on nickel-doped spinel magnesium ferrite nanoparticles for supercapacitor applications, Mater. Chem. Phys. 301 (2023) 127601. https://doi.org/10.1016/j.matchemphys.2023.127601.

[2] M.B. Askari, P. Salarizadeh, Binary nickel ferrite oxide (NiFe2O4) nanoparticles coated on reduced graphene oxide as stable and high-performance asymmetric supercapacitor electrode material, Int. J. Hydrogen Energy. 45 (2020) 27482–27491.

View Article Online
DOI: 10.1039/D5YA00340G

https://doi.org/10.1016/j.ijhydene.2020.07.063.

[3] K.Y. Shih, H.Y. Tseng, One-Step Microwave-Assisted Synthesis of MnFe2O4/rGO Nanocomposites and Their Electrochemical Properties in Supercapacitors, ACS Omega. 10 (2025) 4473–4485. https://doi.org/10.1021/acsomega.4c07810.

[4] N.P. Zentefis, A. Fiore, Y. Yang, Recent Advancements of Spinel Oxide Materials in Energy and Fuel Applications, Energy and Fuels. 39 (2025) 7167–7181. https://doi.org/10.1021/acs.energyfuels.5c00318.

[5] M.K. Zate, S.M.F. Shaikh, V. V. Jadhav, K.K. Tehare, S.S. Kolekar, R.S. Mane, M. Naushad, B.N. Pawar, K.N. Hui, Synthesis and electrochemical supercapacitive performance of nickel-manganese ferrite composite films, J. Anal. Appl. Pyrolysis. 116 (2015) 177–182. https://doi.org/10.1016/j.jaap.2015.09.012.

[6] M. Malarvizhi, S. Meyvel, M. Sandhiya, M. Sathish, M. Dakshana, P. Sathya, D. Thillaikkarasi, S. Karthikeyan, Design and fabrication of cobalt and nickel ferrites based flexible electrodes for high-performance energy storage applications, Inorg. Chem. Commun. 123 (2021) 108344. https://doi.org/10.1016/j.inoche.2020.108344.

[7] S. Shivakumara, T.R. Penki, N. Munichandraiah, High specific surface area α-Fe2O3 nanostructures as high performance electrode material for supercapacitors, Mater. Lett. 131 (2014) 100–103. https://doi.org/10.1016/j.matlet.2014.05.160.

[8] S. K K, A. George, Y.R. Kumar, T. K. K., G. Mandal, A. Chanda, M. Vasundhara, Structural, optical and magnetic properties of pure and 3d metal dopant-incorporated SnO 2 nanoparticles, RSC Adv. 12 (2022) 26712–26726. https://doi.org/10.1039/D2RA03691F.

[9] V. Salve, P. Agale, A. Rokade, M. Kamble, S. Patange, P. More, Zn 1− x Co x Mn 1− x Fe x CrO 4 ferrichromate: an efficient material for high performance supercapacitor applications, New J. Chem. 47 (2023) 20653–20667. https://doi.org/10.1039/D3NJ03295G.

[10] Z. Ansari, S. Kadam, S. Kasabe, J. Tripathi, P. Agale, S. Patange, P. More, Optimized Mn doped ZnO@rGO nanocomposites: a breakthrough for advanced energy storage and PEC systems, Ionics (Kiel). 31 (2025) 8151–8172. https://doi.org/10.1007/s11581-025-06468-x.

611 [11] R. Palm, A.M. Baena-Moncada, J.M. Gonçalves, From medium- to high-entropy
612 hydroxides for hybrid supercapacitors: a review, J. Mater. Chem. A. 12 (2024) 29402–
613 29431. https://doi.org/10.1039/d4ta05625f.

614 [12] M. Pathak, D. Bhatt, R.C. Bhatt, B.S. Bohra, G. Tatrari, S. Rana, M.C. Arya, N.G.
615 Sahoo, High Energy Density Supercapacitors: An Overview of Efficient Electrode
616 Materials, Electrolytes, Design, and Fabrication, Chem. Rec. 24 (2024).
617 https://doi.org/10.1002/tcr.202300236.

618 [13] Z. Ansari, S. Kadam, V. Salve, K. Patil, G. Wadhawa, P. More, Structural,
619 electrochemical, and photoelectrochemical performance of Cr doped ZnO@rGO
620 nanocomposites synthesized via Sol-Gel and hydrothermal methods, J. Mol. Struct.
621 1349 (2026) 143761. https://doi.org/10.1016/j.molstruc.2025.143761.

622 [14] S. Khan, B. Ali, M. Salman, R. Muhammad, M. Khan, F. Hussain, K. Song, D. Wang,
623 Spinel M0.5Zn0.5Fe2O4 (M = Ni, Co, and Cu) ferrites for energy storage applications:
624 Dielectric, magnetic and electrochemical properties, Ceram. Int. 48 (2022) 29291–
625 29297. https://doi.org/10.1016/j.ceramint.2022.05.290.

626 [15] A. Kumar, B.N. Mahanty, A. Rawat, R. Muhammad, R.K. Panigrahi, D. Pradhan, P.
627 Mohanty, Transition-Metal-Substituted Nanoporous Manganese Ferrites
628 Mn0.95M0.05Fe2O4 (M: Co, Cu, and Zn) as Electrode Materials for High-
629 Performance Supercapacitors in Redox-Active Nonaqueous Electrolytes, Energy and
630 Fuels. 37 (2023) 6810–6823. https://doi.org/10.1021/acs.energyfuels.3c00281.

631 [16] K. Xie, J. Li, Y. Lai, W. Lu, Z. Zhang, Y. Liu, L. Zhou, H. Huang, Highly ordered iron
632 oxide nanotube arrays as electrodes for electrochemical energy storage, Electrochem.
633 Commun. 13 (2011) 657–660. https://doi.org/10.1016/j.elecom.2011.03.040.

634 [17] Y. Slimani, M.A. Almessiere, A. Baykal, A.D. Korkmaz, H. Gungunes, S.E. Shirsath,
635 D.S. Klygach, T.I. Zubar, A. V. Trukhanov, L.I. Al-Jumaiah, Fabrication of Nd-Ho
636 Cosubstituted Co0.5Ni0.5Fe2O4 Nanospinel Ferrites and Exploration of Their
637 Microstructure, Magnetic, and Electromagnetic Characteristics, Inorg. Chem. 63
638 (2024) 20749–20761. https://doi.org/10.1021/acs.inorgchem.4c03468.

639 [18] Y. Ma, Y. Ma, Q. Wang, S. Schweidler, M. Botros, T. Fu, H. Hahn, T. Brezesinski, B.
640 Breitung, High-entropy energy materials: Challenges and new opportunities, Energy
641 Environ. Sci. 14 (2021) 2883–2905. https://doi.org/10.1039/d1ee00505g.

View Article Online
DOI: 10.1039/D5YA00340G

[19] Y. Han, M. Tian, C. Wang, T. Zong, X. Wang, High-entropy spinel oxide (Fe0.2Mg0.2Mn0.1Al0.3Cr0.2)3O4 as a highly active and stable redox material for methane driven solar thermochemical water splitting, Appl. Catal. B Environ. 339 (2023) 123096. https://doi.org/10.1016/j.apcatb.2023.123096.

[20] Ö. Başgöz, A. Güngör, Ö. Güler, E. Erdem, High-Entropy Alloys and Oxides as Supercapacitor Electrodes: A Structural and Electrochemical Perspective for Energy Storage, Adv. Sustain. Syst. 9 (2025). https://doi.org/10.1002/adsu.202500201.

[21] C. Wei, Z. Feng, M. Baisariyev, L. Yu, L. Zeng, T. Wu, H. Zhao, Y. Huang, M.J. Bedzyk, T. Sritharan, Z.J. Xu, Valence Change Ability and Geometrical Occupation of Substitution Cations Determine the Pseudocapacitance of Spinel Ferrite XFe2O4(X = Mn, Co, Ni, Fe), Chem. Mater. 28 (2016) 4129–4133. https://doi.org/10.1021/acs.chemmater.6b00713.

[22] H. Dai, R. Zhou, Z. Zhang, J. Zhou, G. Sun, Design of manganese dioxide for supercapacitors and zinc-ion batteries: similarities and differences, Energy Mater. 2 (2022) 200040. https://doi.org/10.20517/energymater.2022.56.

[23] R. Mumtaz, W.H. Shah, Y. Iqbal, H. Ullah, G. Asghar, M. Hussain, M.R. Abukhadra, A.M. El-Sherbeeny, Electrical transport and dielectric relaxation mechanism in Zn0.5Cd0.5Fe2O4 spinel ferrite: A temperature- and frequency-dependent complex impedance study, Heliyon. 10 (2024) e34155. https://doi.org/10.1016/j.heliyon.2024.e34155.

[24] B. Rani, S. Ghosh, N.K. Sahu, A synergistic experimental and computational study on cation engineering in Mn-doped CoFe2O4 nanoparticles for high-performance supercapacitors, Electrochim. Acta. 539 (2025) 147122. https://doi.org/10.1016/j.electacta.2025.147122.

[25] A. Asghar, K. Khan, O. Hakami, W.M. Alamier, S.K. Ali, T. Zelai, M.S. Rashid, A.K. Tareen, E.A. Al-Harthi, Recent progress in metal oxide-based electrode materials for safe and sustainable variants of supercapacitors, Front. Chem. 12 (2024) 1–33. https://doi.org/10.3389/fchem.2024.1402563.

[26] R.S. Salama, M.S. Gouda, M.F.A. Aboud, F.T. Alshorifi, A.A. El-Hallag, A.K. Badawi, Synthesis and characterization of magnesium ferrite-activated carbon composites derived from orange peels for enhanced supercapacitor performance, Sci.

673 Rep. 14 (2024) 1–14. https://doi.org/10.1038/s41598-024-54942-9.

View Article Online
DOI: 10.1039/D5YA00340G

674 [27] K.S. Ganesh, R.R. Gutturu, C.S. Kang, S.W. Joo, Characteristics of nanoparticles of
675 mixed Cu–Zn–Mg spinel ferrites: A study of structural and electrochemical attributes,
676 Ceram. Int. 50 (2024) 6268–6277. https://doi.org/10.1016/j.ceramint.2023.11.352.

677 [28] P. Agale, V. Salve, K. Patil, S. Mardikar, S. Uke, S. Patange, P. More, Synthesis,
678 characterization, and supercapacitor applications of Ni-doped CuMnFeO4 nano
679 Ferrite, Ceram. Int. 49 (2023) 27003–27014.
680 https://doi.org/10.1016/j.ceramint.2023.05.240.

681 [29] Y. Yin, W. Bin Zhang, X.L. Zhang, M.M. Theint, J.L. Yang, Z.Q. Yang, J.J. Li, S.
682 Liang, X.J. Ma, Low-dimensional high entropy oxide (FeCoCrMnNi)3O4 for
683 supercapacitor applications, Dalt. Trans. 52 (2023) 9005–9016.
684 https://doi.org/10.1039/d3dt00909b.

685 [30] T.-E. Hsu, K. Manjunatha, M.-K. Ho, H.-H. Chiu, S.-L. Yu, B.-L. Lyu, Y.-T. Yu, H.-
686 C. Kuo, S.-W. Yu, C.-L. Cheng, S. Matteppanavar, H. Nagabhushana, M.-C. Chen, Y.-
687 L. Huang, S.Y. Wu, High-Performance Bi-Doped NiFe 2 O 4 Nanoparticles for
688 Advanced Supercapacitors and Room-Temperature Magnetic Memory Applications,
689 ACS Appl. Electron. Mater. 7 (2025) 3704–3724.
690 https://doi.org/10.1021/acsaelm.5c00021.

691 [31] F.B. Kadumudi, J. Trifol, M. Jahanshahi, T.-G. Zsurzsan, M. Mehrali, E. Zeqiraj, H.
692 Shaki, M. Alehosseini, C. Gundlach, Q. Li, M. Dong, M. Akbari, A. Knott, K. Almdal,
693 A. Dolatshahi-Pirouz, Flexible and Green Electronics Manufactured by Origami
694 Folding of Nanosilicate-Reinforced Cellulose Paper, ACS Appl. Mater. Interfaces. 12
695 (2020) 48027–48039. https://doi.org/10.1021/acsami.0c15326.

696 [32] S.J.K. T., A. V.R., V. M., A. Muthu, Biosynthesis of multiphase iron nanoparticles
697 using Syzygium aromaticum and their magnetic properties, Colloids Surfaces A
698 Physicochem. Eng. Asp. 603 (2020) 125241.
699 https://doi.org/10.1016/j.colsurfa.2020.125241.

700 [33] Priya, Naveen, K. Kaur, A.K. Sidhu, Green Synthesis: An Eco-friendly Route for the
701 Synthesis of Iron Oxide Nanoparticles, Front. Nanotechnol. 3 (2021).
702 https://doi.org/10.3389/fnano.2021.655062.

[34] Y.R. Kumar, P.E. Prasad, K. Venkataramana, M. Vasundhara, Strategic biotemplating of α-Fe2O3 nanoparticles using egg-derived chelators via sol-gel route: correlated evolution of magnetic, electrical, dielectric and electrochemical properties, Mater. Sci. Eng. B. 323 (2026) 118727. https://doi.org/10.1016/j.mseb.2025.118727.

[35] A. Sunny, K. Venkataramana, Y. Ranjith Kumar, M. Vasundhara, Low and high temperature magnetic properties of MgFe2O4 nanoparticles synthesized by a simple egg white albumin route, J. Cryst. Growth. 662 (2025) 128174. https://doi.org/10.1016/j.jcrysgro.2025.128174.

[36] Y.R. Kumar, P. Trivedi, A. Jana, D. Suman, M. Vasundhara, Preparation of biotemplated Fe 3 O 4 nanoparticles and evaluation of RF-induced heating efficiency for targeted hyperthermia, RSC Adv. 15 (2025) 36879–36894. https://doi.org/10.1039/D5RA03372A.

[37] M.H. Moshafi, M. Ranjbar, G. Ilbeigi, Biotemplate of albumen for synthesized iron oxide quantum dots nanoparticles (QDNPs) and investigation of antibacterial effect against pathogenic microbial strains, Int. J. Nanomedicine. 14 (2019) 3273–3282. https://doi.org/10.2147/IJN.S202462.

[38] R. Lu, Egg white-mediated green synthesis of silver nanoparticles with excellent biocompatibility and enhanced radiation effects on cancer cells, Int. J. Nanomedicine. (2012) 2101. https://doi.org/10.2147/IJN.S29762.

[39] A. V. Singh, B.M. Bandgar, M. Kasture, B.L.V. Prasad, M. Sastry, Synthesis of gold, silver and their alloy nanoparticles using bovine serum albumin as foaming and stabilizing agent, J. Mater. Chem. 15 (2005) 5115–5121. https://doi.org/10.1039/b510398c.

[40] L. Xu, L. Wang, Y. Li, Q. Song, Z. Tian, C. Wang, M. Zhao, N. Gao, A novel high-entropy spinel ferrites (CoNiCuZnMg)Fe2O4 catalyst for H2 production via steam reforming of derived volatiles from polypropylene and waste cooking oil, Chem. Eng. J. 488 (2024). https://doi.org/10.1016/j.cej.2024.150767.

[41] J. Ai, Y. Shuai, M. Hu, L. Cheng, S. Luo, W. Li, Z. Chen, L. Hu, Z. Zhou, Microstructural evolution and catalytic properties of novel high-entropy spinel ferrites MFe2O4 (M= Mg, Co, Ni, Cu, Zn), Ceram. Int. 49 (2023) 22941–22951. https://doi.org/10.1016/j.ceramint.2023.04.119.

View Article Online
DOI: 10.1039/D5YA00340G

[42] K. Sharma, L. Calmels, D. Li, A. Barbier, R. Arras, Influence of the cation distribution, atomic substitution, and atomic vacancies on the physical properties of CoFe2O4 and NiFe2O4 spinel ferrites, Phys. Rev. Mater. 6 (2022) 124402. https://doi.org/10.1103/PhysRevMaterials.6.124402.

[43] K. Patil, S. Kadam, P. Lokhande, S. Balgude, P. More, The effects of cobalt and magnesium co-doping on the structural and magnetic properties of ZnFe2O4 synthesized using a sonochemical process, Solid State Commun. 337 (2021) 114435. https://doi.org/10.1016/j.ssc.2021.114435.

[44] N. Matsubara, T. Masese, E. Suard, O.K. Forslund, E. Nocerino, R. Palm, Z. Guguchia, D. Andreica, A. Hardut, M. Ishikado, K. Papadopoulos, Y. Sassa, M. Månsson, Cation Distributions and Magnetic Properties of Ferrispinel MgFeMnO 4, Inorg. Chem. 59 (2020) 17970–17980. https://doi.org/10.1021/acs.inorgchem.0c02241.

[45] C.M.B. Henderson, J.M. Charnock, D.A. Plant, Cation occupancies in Mg, Co, Ni, Zn, Al ferrite spinels: a multi-element EXAFS study, J. Phys. Condens. Matter. 19 (2007) 076214. https://doi.org/10.1088/0953-8984/19/7/076214.

[46] A.C. Ulpe, K.C.L. Bauerfeind, T. Bredow, Influence of Spin State and Cation Distribution on Stability and Electronic Properties of Ternary Transition-Metal Oxides, ACS Omega. 4 (2019) 4138–4146. https://doi.org/10.1021/acsomega.8b03254.

[47] J.M. Gonçalves, L. V. de Faria, A.B. Nascimento, R.L. Germscheidt, S. Patra, L.P. Hernández-Saravia, J.A. Bonacin, R.A.A. Munoz, L. Angnes, Sensing performances of spinel ferrites MFe2O4 (M = Mg, Ni, Co, Mn, Cu and Zn) based electrochemical sensors: A review, Anal. Chim. Acta. 1233 (2022). https://doi.org/10.1016/j.aca.2022.340362.

[48] P.N. Nikam, S.S. Patil, U.M. Chougale, T.H. Bajantri, A. V. Fulari, V.J. Fulari, Synthesis and characterization of CuFe2O4 spinel ferrite for supercapacitor application, J. Indian Chem. Soc. 101 (2024) 101277. https://doi.org/10.1016/j.jics.2024.101277.

[49] M. Zulqarnain, S.S. Ali, M.A. Yaqub, U. Hira, M.I. Khan, S.A. Aldulmani, R. Ikram, R. Qadir, Synthesis, structural and opto-electrical/electronic trends of Zn/Co substituted spinel ferrites for energy conservation and supercapacitor applications, Mater. Chem. Phys. 322 (2024) 129567.

View Article Online
DOI: 10.1039/D5YA00340G

https://doi.org/10.1016/j.matchemphys.2024.129567.

[50] S.J. Salih, W.M. Mahmood, Review on magnetic spinel ferrite (MFe2O4) nanoparticles: From synthesis to application, Heliyon. 9 (2023) e16601. https://doi.org/10.1016/j.heliyon.2023.e16601.

[51] B. Talluri, M.L. Aparna, N. Sreenivasulu, S.S. Bhattacharya, T. Thomas, High entropy spinel metal oxide (CoCrFeMnNi)3O4 nanoparticles as a high-performance supercapacitor electrode material, J. Energy Storage. 42 (2021) 103004. https://doi.org/10.1016/j.est.2021.103004.

[52] A. Manohar, T. Suvarna, S. V. Prabhakar Vattikuti, D. Kim, S. Sangaraju, B.A. Al-Asbahi, K.H. Kim, Zn0.5MgxCu0.5-xFe2O4 spinel ferrites as electrode materials for supercapacitor applications, Inorg. Chem. Commun. 177 (2025) 114393. https://doi.org/10.1016/j.inoche.2025.114393.

[53] R. Bhosale, S. Bhosale, V. Chavan, C. Jambhale, D.K. Kim, S. Kolekar, Hybrid Supercapacitors Based on Nanoporous Carbon and CoFe2O4 Derived from a Bimetallic Organic Framework, ACS Appl. Nano Mater. 7 (2024) 2244–2257. https://doi.org/10.1021/acsanm.3c05664.

[54] R.C. Pullar, Hexagonal ferrites: A review of the synthesis, properties and applications of hexaferrite ceramics, Prog. Mater. Sci. 57 (2012) 1191–1334. https://doi.org/10.1016/j.pmatsci.2012.04.001.

[55] S.H.T. Zim, M.N.R. Naim, M.A. Hossain, M.S. Sikder, Investigation of calcination temperature effect on crystallographic, morphological, optical, and magnetic properties of silver-doped magnesium ferrite nanoparticles, Next Nanotechnol. 7 (2025) 100140. https://doi.org/10.1016/j.nxnano.2025.100140.

[56] Marcus Einert, 2023 - Einert - Sol-Gel-Derived Ordered Mesoporous High Entropy Spinel Ferrites and Assessment of Their.pdf, (2023).

[57] M.L. Aparna, A.N. Grace, P. Sathyanarayanan, N.K. Sahu, A comparative study on the supercapacitive behaviour of solvothermally prepared metal ferrite (MFe2O4, M = Fe, Co, Ni, Mn, Cu, Zn) nanoassemblies, J. Alloys Compd. 745 (2018) 385–395. https://doi.org/10.1016/j.jallcom.2018.02.127.

[58] I.F.F. Christopher, A. Karuppiah, Preparation of spinel ferrites-based flexible

electrodes for high electrochemical performances, Chem. Phys. Impact. 8 (2024) 100460. https://doi.org/10.1016/j.chphi.2024.100460.

[59] N.Y. Elamin, A. Modwi, W. Abd El-Fattah, A. Rajeh, Synthesis and structural of Fe3O4 magnetic nanoparticles and its effect on the structural optical, and magnetic properties of novel Poly(methyl methacrylate)/ Polyaniline composite for electromagnetic and optical applications, Opt. Mater. (Amst). 135 (2023) 113323. https://doi.org/10.1016/j.optmat.2022.113323.

[60] A. Rai, A.K. Thakur, Effect of co-substitution on structural, optical, dielectric and magnetic behavior of LaFeO3, J. Alloys Compd. 695 (2017) 3579–3588. https://doi.org/10.1016/j.jallcom.2016.11.407.

[61] S. Chakrabarty, S. Bandyopadhyay, M. Pal, A. Dutta, Sol-gel derived cobalt containing Ni–Zn ferrite nanoparticles: Dielectric relaxation and enhanced magnetic property study, Mater. Chem. Phys. 259 (2021) 124193. https://doi.org/10.1016/j.matchemphys.2020.124193.

[62] A. Zaman, A. Ali, H. Shahid, S.H. Alrefaee, S. Knani, V. Tirth, A. Algahtani, N. Elboughdiri, Study on the structural, optical, vibrational and dielectric properties of Cr 2+ -doped SnFe 2 O 4 spinel ferrites, RSC Adv. 15 (2025) 37050–37061. https://doi.org/10.1039/D5RA05190H.

[63] M. Méndez-Galván, C.L. Ordoñez-Romero, H.A. Lara-García, G. Díaz, Tailoring band gap and light absorption in M-TiNT (M = Cu2+, Ni2+, Co2+, and Fe3+) for water remediation, J. Nanoparticle Res. 27 (2025) 267. https://doi.org/10.1007/s11051-025-06453-5.

[64] V. Kumar, C.R. Mariappan, R. Azmi, D. Moock, S. Indris, M. Bruns, H. Ehrenberg, G. Vijaya Prakash, Pseudocapacitance of Mesoporous Spinel-Type MCo 2 O 4 (M = Co, Zn, and Ni) Rods Fabricated by a Facile Solvothermal Route, ACS Omega. 2 (2017) 6003–6013. https://doi.org/10.1021/acsomega.7b00709.

[65] G. Lee, G. Park, S.S. Park, Molecular-Level Pore Tuning in 2D Conductive Metal-Organic Frameworks for Advanced Supercapacitor Performance, J. Am. Chem. Soc. 146 (2024) 29767–29772. https://doi.org/10.1021/jacs.4c11372.

[66] S. Lalwani, R.B. Marichi, M. Mishra, G. Gupta, G. Singh, R.K. Sharma, Edge

enriched cobalt ferrite nanorods for symmetric/asymmetric supercapacitive charge storage, Electrochim. Acta. 283 (2018) 708–717. https://doi.org/10.1016/j.electacta.2018.07.008.

[67] K. Malaie, M.R. Ganjali, Spinel nano-ferrites for aqueous supercapacitors; linking abundant resources and low-cost processes for sustainable energy storage, J. Energy Storage. 33 (2021) 102097. https://doi.org/10.1016/j.est.2020.102097.

[68] Z. Batool, Z. Ali, A. ur Rehman, M.A. ul Haq, N.H. Alotaibi, S.M. Wabaidur, N. Ahmad, Exploring different non-iron based Co-spinel ferrites as potential electrode materials for supercapacitor applications, J. Energy Storage. 92 (2024) 112129. https://doi.org/10.1016/j.est.2024.112129.

[69] A. Ghazal, A.C. Mendhe, A. Kore, S. Dhas, R. Batool, D. Kim, Enhanced performance of CoFe2O4 supercapacitors through synergistic interaction of Co2+ and Fe2+, J. Energy Storage. 104 (2024) 114584. https://doi.org/10.1016/j.est.2024.114584.

[70] A.E. Elkholy, F. El-Taib Heakal, N.K. Allam, Nanostructured spinel manganese cobalt ferrite for high-performance supercapacitors, RSC Adv. 7 (2017) 51888–51895. https://doi.org/10.1039/c7ra11020k.

[71] A. Murugan, V. Siva, A. Shameem, R. Deepika, S. Bharathkumar, H. Valdés, S.A. Bahadur, Electrochemical properties of nanoscale Cu[sbnd]Co spinel ferrite system: A promising positive electrode for high performance supercapacitors, J. Energy Storage. 99 (2024). https://doi.org/10.1016/j.est.2024.113179.

[72] E.P. P., Y.R. Kumar, S.D. Jagadale, C.R.K. Rao, S. V. Bhosale, Exploration of acid-doped polyureas with redox-active aniline oligomers for supercapacitor applications, Mater. Sci. Energy Technol. 8 (2025) 231–242. https://doi.org/10.1016/j.mset.2025.07.002.

[73] B. Bhujun, M.T.T. Tan, A.S. Shanmugam, Study of mixed ternary transition metal ferrites as potential electrodes for supercapacitor applications, Results Phys. 7 (2017) 345–353. https://doi.org/10.1016/j.rinp.2016.04.010.

[74] B. Bhujun, M.T.T. Tan, A.S. Shanmugam, Evaluation of aluminium doped spinel ferrite electrodes for supercapacitors, Ceram. Int. 42 (2016) 6457–6466. https://doi.org/10.1016/j.ceramint.2015.12.118.

[75] B. Jeevanantham, D. Vignesh, M.K. Shobana, T. Pazhanivel, R. Thangappan, S. Kavita, Theoretical and Experimental Insights of Magnesium-doped Cobalt Ferrites for Supercapacitor Applications, Electrochim. Acta. 470 (2023) 143309. https://doi.org/10.1016/j.electacta.2023.143309.

[76] S. Azizi, M.B. Askari, S.M. Rozati, M. Masoumnezhad, Nickel ferrite coated on carbon felt for asymmetric supercapacitor, Chem. Phys. Impact. 8 (2024) 100543. https://doi.org/10.1016/j.chphi.2024.100543.

[77] S.J. Uke, S.P. Mardikar, D.R. Bambole, Y. Kumar, G.N. Chaudhari, Materials Science for Energy Technologies Sol-gel citrate synthesized Zn doped MgFe 2 O 4 nanocrystals : A promising supercapacitor electrode material, Mater. Sci. Energy Technol. 3 (2020) 446–455. https://doi.org/10.1016/j.mset.2020.02.009.

[78] A. Manohar, K. Chintagumpala, S.V.P. Vattikuti, B.A. Al-Asbahi, N. Mameda, K.H. Kim, CaxZn0.5-xMg0.5Fe2O4 nanoparticles: A novel approach for supercapacitor applications, Mater. Chem. Phys. 336 (2025) 130518. https://doi.org/10.1016/j.matchemphys.2025.130518.

View Article Online
DOI: 10.1039/D5EA00340G

The data [e.g., raw data, characterization data, or analytical methods] supporting the findings of this study are available with the corresponding author. Data can be obtained from the corresponding author upon reasonable request.